

1 **Title:**

2 Discretely Assembled Mechanical Metamaterials

3 **Authors:**

4 Benjamin Jenett^{1*}, Christopher Cameron², Filippos Tournomousis¹, Alfonso Parra Rubio¹, Megan
5 Ochalek¹, Neil Gershenfeld¹

6 **Affiliations:**

7 ¹*Center for Bits and Atoms, Massachusetts Institute of Technology, Cambridge, MA*

8 ²*U.S. Army Research Laboratory, Aberdeen Proving Ground, MD*

9 *corresponding author bej@mit.edu

10 **Abstract:**

11 Mechanical metamaterials offer novel properties based on local control of cell geometry and their
12 global configuration into structures and mechanisms. Historically, these have been made as
13 continuous, monolithic structures with additive manufacturing, which affords high resolution and
14 throughput, but is inherently limited by process and machine constraints. To address this issue, we
15 present a construction system for mechanical metamaterials based on discrete assembly of a
16 finite set of parts, which can be spatially composed for a range of properties such as rigidity,
17 compliance, chirality, and auxetic behavior. This system achieves desired continuum properties
18 through design of the parts such that global behavior is governed by local mechanisms. We
19 describe the design methodology, production process, numerical modeling, and experimental
20 characterization of metamaterial behaviors. This approach benefits from incremental assembly,
21 which eliminates scale limitations, best-practice manufacturing for reliable, low-cost part
22 production, and interchangeability through a consistent assembly process across part types.

23
24 **MAIN TEXT**

25

26 **Introduction**

27 The notion of rationally designing a material from the micro to the macro scale has been a
28 longstanding goal with broad engineering applications. By controlling local cell properties and
29 their global spatial distribution and arrangement, metamaterials with novel behavior can be
30 achieved. The foundation for mechanical metamaterials comes from the study of cellular solids

31 (1), where natural materials such as wood and bone (2), or synthetic materials such as stochastic
32 foams, are understood as a network of closed or open cells (3). In the latter case, edges form a
33 network of beams, and based on the connectivity of these beams and their base material,
34 macroscopic behaviors can be predicted analytically (4). It was from this insight that the field of
35 architected materials formed, enabling design of periodic structures with tailorable properties
36 such as improved stiffness over foams due to higher degrees of connectivity (5).

37 Advances in digital fabrication, specifically, additive manufacturing, have enabled these
38 complex designs to be realized. Seminal work demonstrated stiff, ultralight lattice materials (6),
39 and has since been improved, resulting in mechanical metamaterials with superior stiffness and
40 strength at ultralight densities (7) with multiscale hierarchy (8). Benefits of nanoscale features
41 further expand the exotic property parameter space (9) and architectures featuring closed-cell
42 plates have shown potential for approaching the theoretical limit for elastic material performance
43 (10). Other designs seek to utilize compliance, which can be attained through internal geometric
44 mechanisms (11), or through base materials capable of large strain (12). Internal architectures can
45 be designed to transmit or respond to load in other non-standard ways. Auxetic metamaterials
46 exhibit zero or negative Poisson's ratio (13). Internal, re-entrant architectures produce contraction
47 perpendicular to compressive loading, and expansion perpendicular to tensile loading, counter to
48 traditional continuum material behavior (14). Chiral metamaterials exhibit handedness based on
49 asymmetric unit cell geometry. These designs produce out of plane deformations, such as twist, in
50 response to in plane loading (15).

51 Nearly all of the aforementioned mechanical metamaterials are made with some form of
52 additive manufacturing, most of which are summarized in (16). These processes vary widely in
53 terms of cost, precision, throughput, and material compatibility. The lower end of the cost
54 spectrum, such as fused deposition modeling (FDM), also tends to have lower performance.
55 Limits of thermoplastic extrusion include layer-based anisotropy (17) and errors resulting from
56 build angles for complex 3D geometry (18). Higher performance, and higher cost, processes such
57 as selective laser melting (SLM) utilize materials such as stainless steel, but require non-trivial
58 setup for particulate containment, and can suffer from layer-based anisotropy, thermal warping,
59 and geometry irregularity (19). Some of the highest performance multi-scale metal microlattice
60 production techniques based on lithographic and plating processes are well-studied and repeatable
61 but are also highly specialized and labor-, time-, and cost-intensive. Polymerization, curing,
62 plating, milling, and etching can require up to 24 hours from start to finish for sample preparation
63 (6). Large area projection microstereolithography (LAP μ SL) is capable of producing lattices with
64 μm (10^{-6} m) scale features on centimeter (10^{-2} m) scale parts (8) with significantly improved

65 throughput, but extension to macro-scale ($>1\text{m}$) structures remains out of reach, due to practical
66 limitations in scaling these processes and their associated machines.

67 The largest structure that can be printed with any given process is typically limited by the
68 build volume of the machine. Therefore, significant effort is focused on scaling up the machines.
69 Meter-scale FDM platforms (20) and larger cementitious deposition machines (21) have been
70 demonstrated, and coordinated mobile robots are proposed to achieve arbitrarily large work areas
71 (22). However, there is a tradeoff between precision, scale, and cost. Commercially available two-
72 photon polymerization machines have resolution on the order of $1\ \mu\text{m}$ ($10^{-6}\ \text{m}$), build size on the
73 order of 100mm ($10^{-1}\ \text{m}$), and cost on the order of $10^6\ \text{\$/machine}$ (23). Macro-scale FDM
74 machines boast build sizes of $10^1\ \text{m}$ (24), but are unlikely to have sub-mm ($10^{-3}\ \text{m}$) resolution.
75 Thus, roughly the same dynamic range (scale/resolution) is offered, but with costs approaching
76 $10^7\ \text{\$/machine}$, we see a possible super-linear cost-based scaling of achievable dynamic range.
77 Building large, precise machines is expensive, and due to the inherent coupling of machine
78 performance, size, and cost, there are significant challenges for realizing macro-scale ($>1\text{m}$)
79 mechanical metamaterials with high quality and low cost.

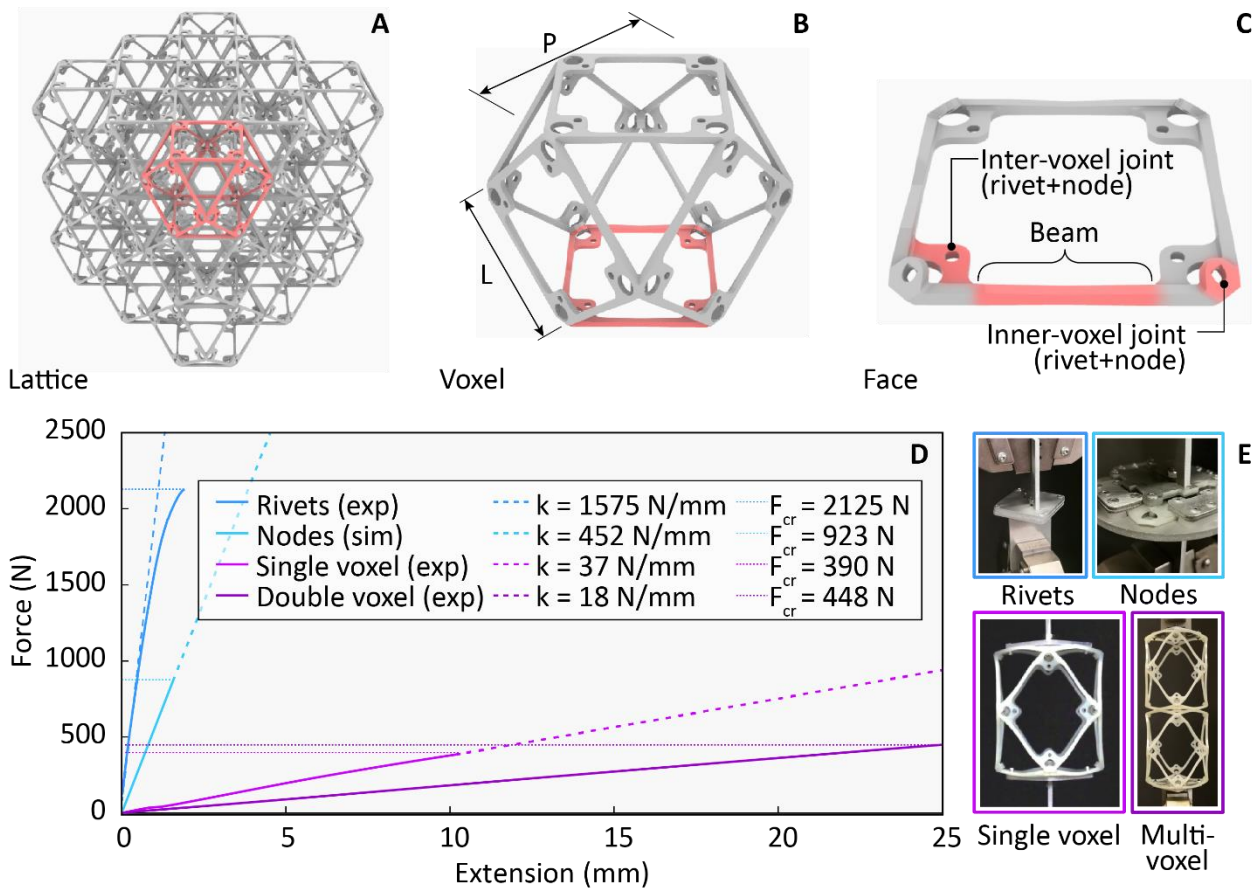
80 An alternative approach to producing mechanical metamaterials seeks to decouple these
81 aspects, and in doing so overcome machine-based limitations. Based on reversible assembly of
82 discrete, modular components, this method utilizes mechanical connections to build larger,
83 functional metamaterials and structures out of smaller, mass producible parts. The first
84 demonstration of this approach utilized custom wound, centimeter-scale, carbon fiber reinforced
85 polymer (CFRP) components (25), resulting in an ultralight density lattice with improved elastic
86 stiffness performance over then state of the art metallic microlattice (6), due to the high modulus
87 constituent material. Following this, larger scale, octahedral voxel (volumetric pixel) building
88 block units were made using commercial off the shelf (COTS) high modulus, unidirectional
89 pultruded CFRP tubes connected with injection molded glass fiber reinforced polymer (GFRP)
90 nodes, resulting in a macro-scale ($>1\text{m}$), high performance, reconfigurable structure system (26).
91 Following this, entire voxel units were made with injection molding of GFRP, yielding the first
92 truly mass-producible discrete lattice material system with low cost, best-practice repeatability,
93 and high performance (27). Discrete assembly offers scalability and functionality not achievable
94 with traditional methods due to process and machine limitations.

95 In this paper, we present a construction system for mechanical metamaterials based on
96 discrete assembly of a finite set of modular, mass produced parts. We demonstrate experimentally
97 the desired metamaterial property for each part type, and combined with numerical modeling
98 results, display other novel, unexpected properties. A modular construction scheme enables a

99 range of mechanical metamaterial properties to be achieved, including rigid, compliant, auxetic
 100 and chiral, all of which are assembled with a consistent process across part types, thereby
 101 expanding the functionality and accessibility of this approach. The incremental nature of discrete
 102 assembly enables mechanical metamaterials to be produced efficiently and at low cost, beyond
 103 the scale of the 3D printer.

105 Results

106 *Continuum behavior from discrete parts*



109 **Figure 1: Continuum behavior from discrete parts: subsystem description and characterization.**

110 A) 3x3x3 lattice consists of 27 individual voxels, B) Voxels consist of six individual faces, C)
 111 Faces consist of beams and joints, D) Experimental results for subsystem characterization, where
 112 we see joints (rivets + nodes) are individually stiffer and stronger than voxels, which are
 113 governed by beam properties E) Subsystem testing setups.

114 First, we present the discrete material construction system and show how continuum
 115 behavior is achieved through design of the parts and their relative structural performance. Parts

116 are designed to have their local beam properties govern global lattice behavior, resulting in an
117 effective bulk material that behaves as if it were produced monolithically, so that, structurally
118 speaking, the joints disappear.

119 A lattice, or a mechanical metamaterial consisting of a periodic network of interconnected
120 beams, can be described, and its performance predicted, analytically. We can describe lattices as
121 stretch- or bending-dominated, based on how they resolve external forces as a function of their
122 internal beam connectivity, which corresponds to Maxwell's frame rigidity criteria extended to
123 3D (5). Stretch-dominated lattices, such as the octet, have higher connectivity ($Z = 12$) and higher
124 stiffness to weight than bending-dominated lattices, such as the kelvin, which have lower
125 connectivity ($Z = 4$) (7). In this work we use the cuboctahedra lattice (referred to as Cuboct)
126 geometry, which is uniquely positioned between low and high connectivity ($Z = 8$) yet has been
127 shown to have stretch-dominated behavior, in both microlattice implementation (28) and as
128 discretely assembled vertex connected octahedra (27).

129 In Figure 1A-C, we show a new decomposition using face-connected cuboctahedra voxels
130 which produces the same lattice geometry but has additional benefits to be discussed herein.
131 Voxels are discretized into faces, which consist of beams and joints. There are two types of joints:
132 inner-voxel joints are the points at which 6 separate faces are joined to form a voxel, and inter-
133 voxel joints provide the vertex to vertex connections between neighboring voxels at along a single
134 face. A joint consists of nodes, which are the geometric features on the part providing the
135 fastening area, and the fasteners, which are mechanical connectors. Based on the material and
136 geometric properties of each subsystem, local properties can be controlled to ensure proper
137 global, continuum behavior. In this case, our lattice should behave as an interconnected network
138 of beams. Therefore, we wish to design joints to possess significantly higher effective stiffness
139 and strength than the beams they connect. In this way, the global effective stiffness and strength
140 of the lattice are governed by those subsystems with the lowest relative value.

141 Following as-molded material characterization to calibrate analytical and numerical
142 models (Figure S1), subsystems are then characterized in tests designed to isolate the critical
143 performance aspects for proper system behavior. Rivets, inter-voxel nodes, individual voxels
144 (consisting of beams and inner-voxel joints), and multi-voxel assemblies were tested. The specific
145 goal is to quantify the degree to which voxel and multi-voxel behavior is governed by stiffness
146 and strength properties of the beams, rather than the joints. Experimental results are shown in
147 Figure 1D, with axial stiffness and critical load values noted.

148 Since each subsystem effectively acts across the same cross section (a single voxel), we
149 can directly compare their yield strength using their observed failure loads. We see the intervoxel

150 node and fastener yield strengths are roughly two and four times the voxel yield strength,
151 respectively. For axial stiffness, we treat single and multi-voxel tests as effective springs in series.
152 A single voxel then consists of five effective springs in series: top fasteners, top nodes, voxel,
153 bottom nodes, and bottom fasteners. For springs in series, the equivalent axial stiffness is the
154 reciprocal of the sum of the individual spring reciprocals:

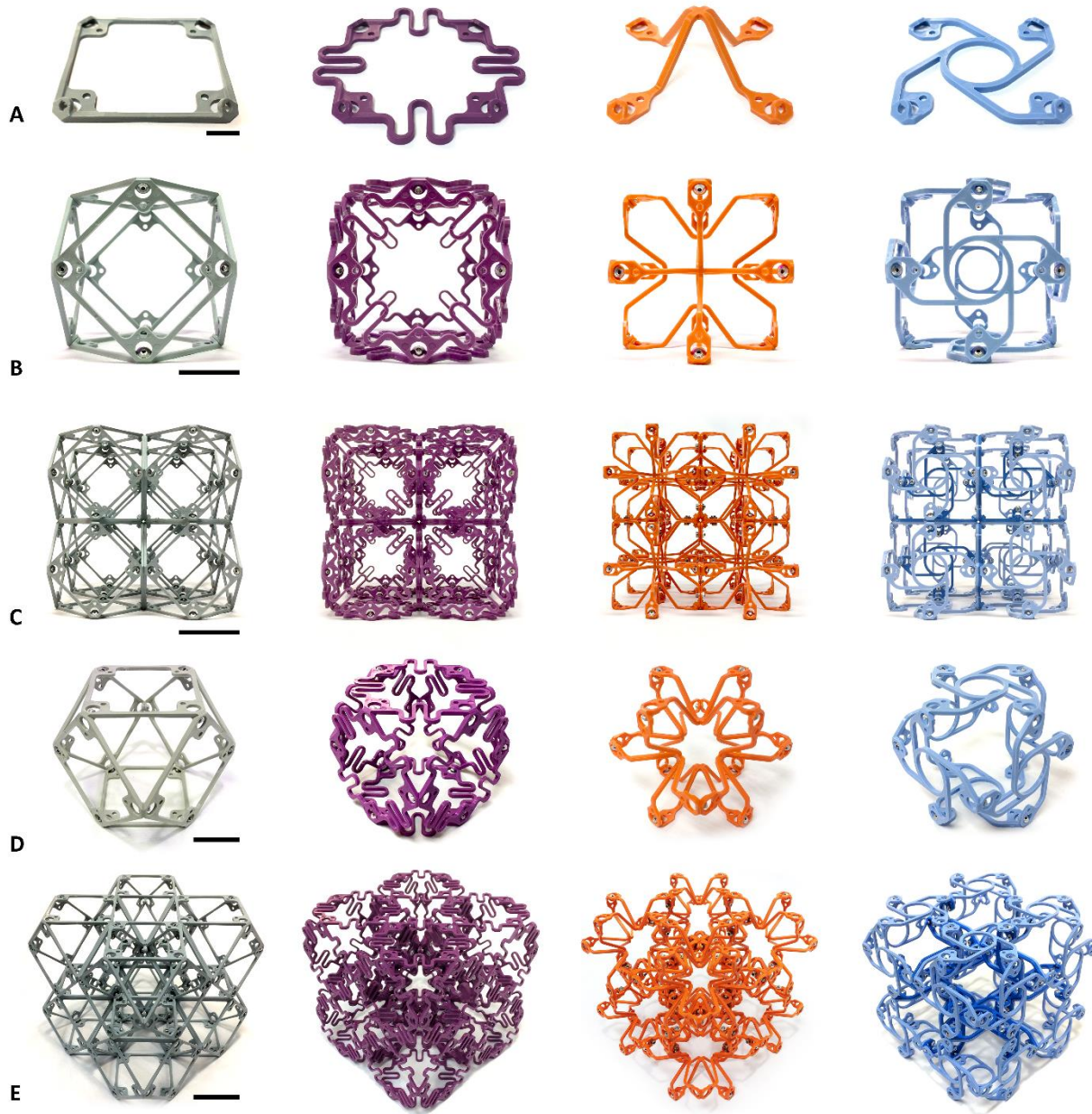
$$\frac{1}{k_{eq}} = \sum_{i=1}^n \frac{1}{k_i}$$

$$k_1 \ll k_{i>1}$$

$$k_{eq} \approx k_1$$

155
156
157
158 For large k_i and small k_1 , we see that k_{eq} equals k_1 , indicating that the governing value is
159 the lower spring stiffness. Using measured values for fasteners, nodes, and voxels, we see the
160 experimental value for the two-voxel assembly agrees with this analytical description, and that
161 both effective stiffness and strength are governed by voxel, and thus beam, properties. This
162 construction system is then used to design a family of part types with a range of mechanical
163 metamaterial properties.

164
165
166
167



169

170 **Figure 2: Four types of discretely assembled mechanical metamaterials, left to right: rigid,**
 171 **compliant, auxetic, and chiral.** A) As-molded face parts, B) Single voxel, front view, C) 2x2x2
 172 Cube, front view, D) Single voxel, oblique view, E) 2x2x2 oblique view. Scale bars: A) 10mm, B,
 173 D) 25mm, C, E) 50mm.

174

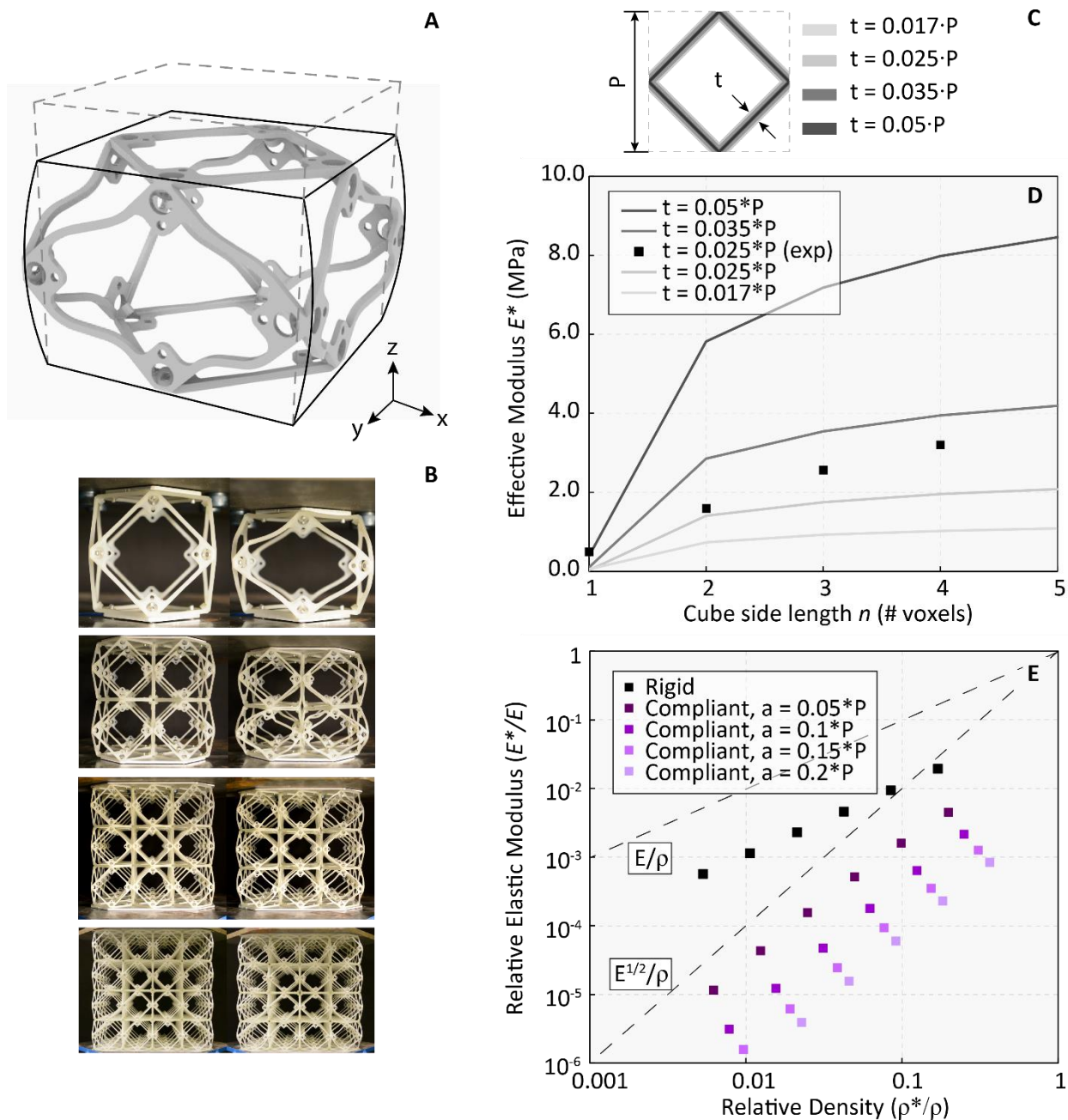
175 Here we present the discretely assembled mechanical metamaterial system consisting of
176 four part types: rigid, compliant, auxetic, and chiral, shown in Figure 2. Six face parts (Figure 2A)
177 are assembled to form voxels (Figure 2B), which are then assembled to form multi-voxel lattices
178 (Figure 2C). Details of the assembly procedure and throughput metrics can be found in
179 Supplementary materials.

180 Rigid voxels resolve external loading through axial beam tension and compression, resulting
181 in elastic, followed by plastic, buckling of struts. Lattice made with these parts shows near-linear
182 scaling of effective modulus, positive Poisson ratio, and yield strength determined by
183 manufacturing process parameters. Compliant voxels are designed with corrugated flexure beams,
184 a motif found in flexural motion systems (29), which resolve axial beam forces through elastic
185 deformation of the planar flexures. Lattice made with these parts show consistent elastomeric
186 behavior at even single voxel resolution and have a near-zero Poisson ratio. Auxetic voxels are
187 designed as intersecting planes of re-entrant mechanisms, which expand and contract laterally under
188 uniaxial tension and compression, respectively. Lattice made with these parts show negative
189 Poisson ratio through a combined action of pure mechanism and flexural beam bending. Chiral
190 voxels are designed with an asymmetric mechanism which responds to in plane loading by
191 producing either clockwise (CC) or counterclockwise (CCW) rotation. When interconnected in
192 three dimensions, this produces out of plane twist in response to uniaxial tension or compression.
193 By combing CC and CCW parts, internal mechanism frustration can be avoided, enabling improved
194 scalability over prior art. The four lattice types and their behaviors will be described in further detail
195 in the following subsections.

196

197

198



200

201 **Figure 3: Rigid mechanical metamaterial.** A) Characteristic unit cell voxel demonstrating beam
 202 buckling and positive transverse strain in response to compressive load, B) Experimental test
 203 setup for $n = 1-4$, undeformed (L), and at initial beam failure (R), C) Geometric parameters for
 204 simulations, where beam thickness t is a function of lattice pitch P , D) Effective stiffness
 205 simulation and experimental results demonstrating continuum behavior at increasing voxel count
 206 E) Simulation results for modulus-density scaling value for rigid and compliant lattice, which are
 207 linear and quadratic, respectively.

208

209
210
211
212
213
214
215
216
217
218
219
220
221
222
223
224
225
226
227
228
229
230
231
232
233
234
235
236
237
238
239
240
241

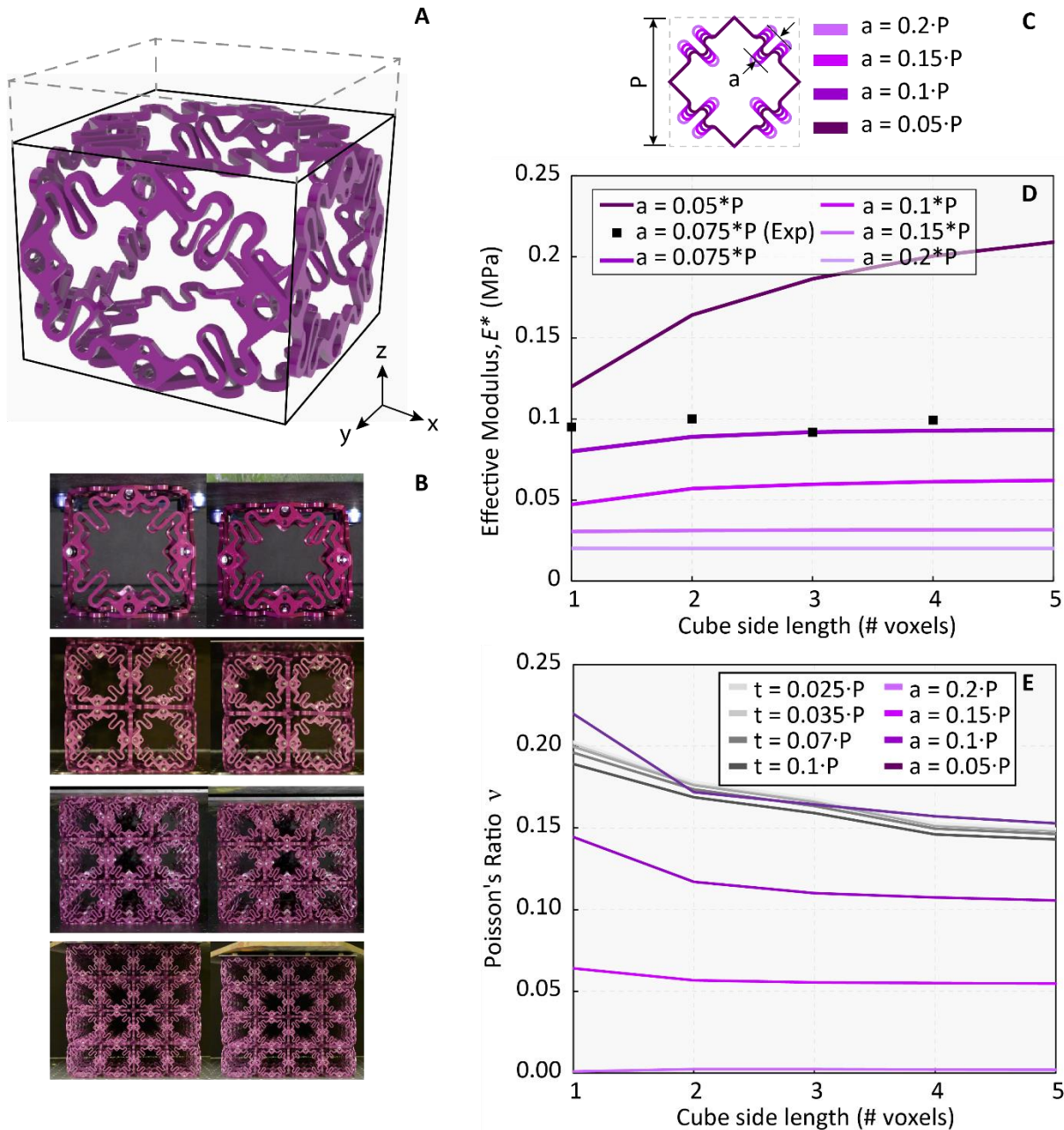
The rigid lattice type exhibits modulus-density scaling which matches previous results in literature but does so with a novel geometric decomposition. We present experimental and numerical results for the rigid lattice type in Figure 3. The characteristic behavior of a unit cell voxel is shown in Figure 3A. The geometry is isotropic along its primary axes, and it responds to loads through axial beam tension and compression. While individual voxels are dominated by under-constrained, mechanism behavior of the quadrilateral faces, when multiple voxels are joined, there is sufficient connectivity to provide rigidity through triangulation of neighboring voxel faces. As a result, effective modulus increases with increasing cell count, and this value eventually reaches an effective continuum value, as seen in Figure 3D.

Having established that the global behavior is governed by the beam properties, now we can correlate analytical models with experimental results for effective lattice behavior. Here we will look at effective elastic modulus E^* and yield strength σ_y , the former corresponding to the linear portion of the stress strain curve under quasi-static loading, and the latter corresponding to the failure load divided by the specimen cross section area. Stress-strain curves for lattice specimens of cube side voxel count $n = 1-4$ are shown in Figure S7, where an initial linear elastic regime is followed by a non-linear elastic regime and plastic yield. Using load and displacement data, stress and strain values are calculated based on lattice specimen size. The calculated moduli are shown with numerical results in Figure 3D. It can be seen that as voxel count n increases, E^* approaches a continuum value depending on the beam thickness, and thus relative density of the lattice. Numerically, we investigate the effect of increasing beam thickness t as a function of lattice pitch P and plot the resulting curves in Figure 3D.

These predicted effective lattice properties over the range of effective densities are plotted relative to constituent values in Figure 3E. The slope of the curve connecting these points, plotted on a log/log chart, provides the power scaling value, which is used to analytically predict lattice behaviors at the macroscopic scale (4). Effective modulus and density are related to constituent modulus and density by $E^*/E \propto (\rho^*/\rho)^a$, where a is 1 for stretch dominated lattices and 2 for bending dominated. We find $a = 1.01$ for our rigid lattice. Based on the agreement between experimental and numerical results, we can conclude that the linear scaling shown is valid. This scaling value had been shown previously for the monolithic (additively manufactured) cuboctahedron lattice (28) and for discretely assembled, vertex connected octahedra (27), to which we now add our novel lattice decomposition.

242 Next, we compare experimental yield stress results with analytical predictions of local
243 beam failure based on relative density, as a function of beam thickness t and lattice pitch P . Here,
244 we will use experimental data from the 4x4x4 specimen, as this is closest to demonstrating
245 continuum behavior. Based on the load at failure and lattice geometry, we can determine a given
246 beam compressive failure load to be 88N. We determine the analytical critical beam load using
247 either the Euler buckling formula or the Johnson parabola limit, depending on the compression
248 member's slenderness ratio (Figure S3). We determine our beam slenderness ratio to be 29.5,
249 which is over the critical slenderness ratio of 19.7 (see supplementary material for complete
250 calculation), thus we use Euler buckling formula. Because the as-molded material properties vary,
251 we determine the critical load to range from 70 to 108 N, with the mean value of 89 N very
252 closely approximating the experimental value. Thus, we see good correlation between both
253 stiffness and strength based on the design of our discrete lattice material.

254
255
256
257
258



260

261 **Figure 4: Compliant mechanical metamaterial.** A) Characteristic unit cell voxel demonstrating
 262 flexure spring-beam deformation and small transverse strain in response to compressive load, B)
 263 Experimental test setup for $n = 1-4$, undeformed (L), and at onset of non-linearity (R), C)
 264 Geometric parameters for simulations, where spring-beam amplitude a is a function of lattice
 265 pitch P , D) Effective stiffness simulation and experimental results, which show near continuum
 266 value at low voxel count for all but the smallest spring-beam amplitude designs, E) Simulation
 267 results for effective Poisson's ratio for rigid and compliant lattice, with large spring-beam
 268 amplitudes having a value of near zero.

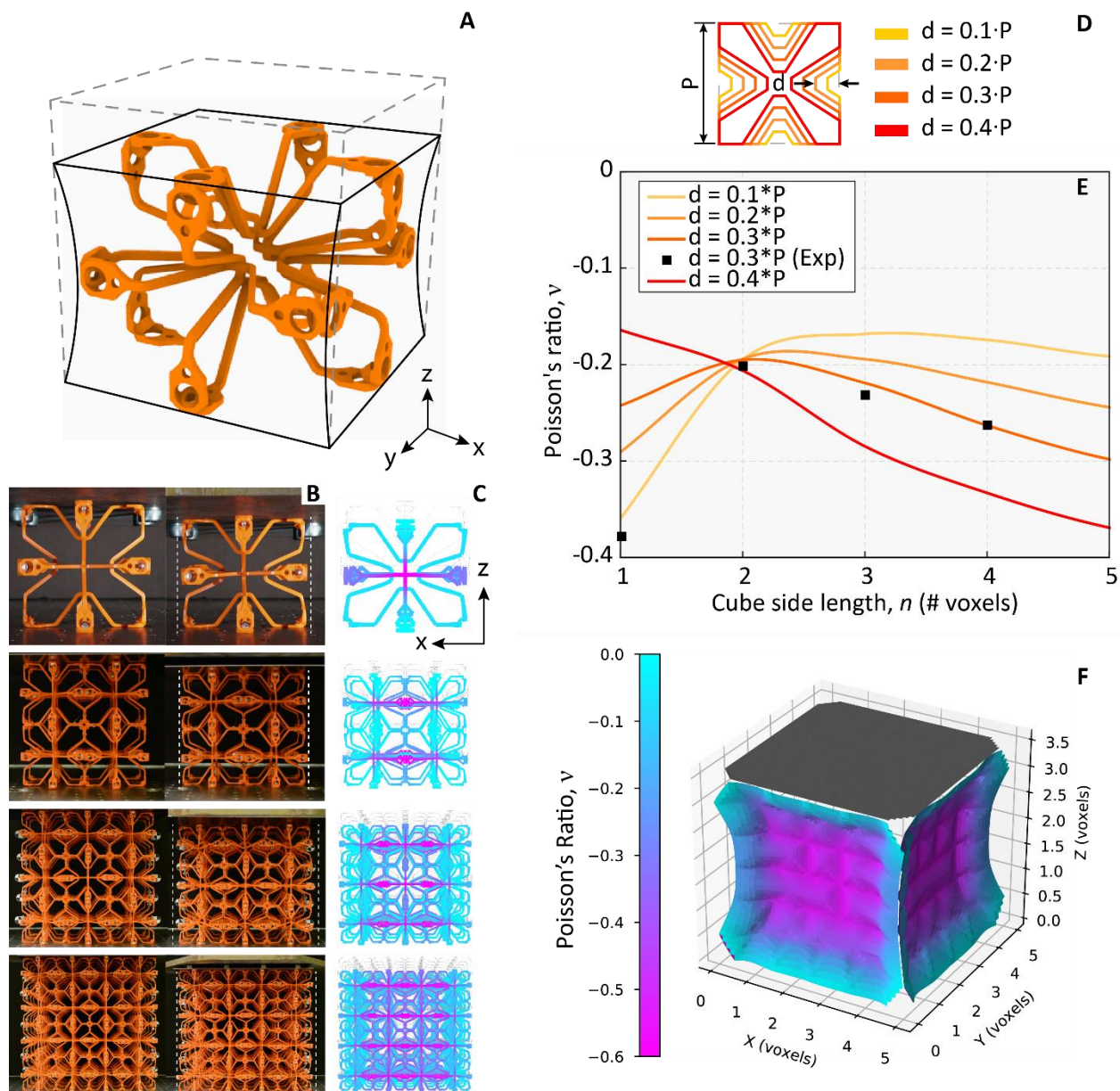
269 The compliant lattice type exhibit quadratic scaling for effective stiffness, as well as
270 consistency across voxel counts regarding continuum behavior and elastic limit values. We
271 present experimental and numerical results for the compliant lattice type in Figure 4. The
272 characteristic behavior of a unit cell voxel is shown in Figure 4A. While the load paths are
273 topologically the same as the rigid voxel, as this is a function of lattice connectivity, the
274 mechanism through which beams resolve these loads is different. Here, the planar-spring beams
275 deform in combined axial and in-plane bending, as a controllable property of the compliant
276 features we design. This produces several unique properties in this lattice type.

277 First, we can see from the experimental stress-strain curves that for similar strains, the
278 compliant lattice shows linear elastic behavior, up until the elastic limit (Figure S7-B). The stress
279 at which this transition occurs is consistent across voxel counts, from $n = 1$ to $n = 4$. Second, the
280 effective modulus is also consistent across voxel counts. This is confirmed by simulations, as
281 shown in Figure 4D. Given the large range of linear to non-linear and individual to continuum
282 behavior seen in the rigid lattice, the compliant lattice is markedly different in its consistency.
283 This behavior is attributable to the spring-like behavior of the beams, a similar observation to
284 analytical models for stochastic foams (30). As cube specimen side length voxel count increases,
285 so do the number of springs acting in parallel, which produces an effective spring stiffness
286 $K_{eff} = K_1 + K_2 + K_n \dots$. But as spring count increases, so does effective area, both proportional
287 to side length squared. Thus, a single voxel has the same effective modulus as a 4x4x4 or an $n \times n$
288 $\times n$ cube. This effect is reduced as beam-spring amplitude a goes to zero, meaning it approaches
289 behavior similar to the rigid cuboct lattice.

290 Another property observed experimentally, and confirmed numerically, is a low, near-
291 zero, Poisson's ratio. Figure 4E shows the simulated effective Poisson's ratios for the compliant
292 and rigid voxel. At the largest compliant amplitude, we see a value of near zero. As the amplitude
293 a of the compliant spring feature goes to zero, the Poisson's ratio converges to around 0.15, which
294 is the effective value for the entire parameter range of the rigid lattice.

295 Finally, this lattice shows near quadratic stiffness scaling, in contrast to the near linear
296 scaling shown by the rigid lattice, while having the same base lattice topology and connectivity as
297 the rigid version (Figure 3E)—meaning it has bending-dominated behavior with a stretch
298 dominated lattice geometry. This is attributable to the localized behavior of the spring-like beams.
299 Whereas in the rigid lattice vertically oriented beams in compression are offset by horizontally
300 oriented beams in tension, resulting in stretch dominated behavior, here global strain is a function
301 of local spring-beam strain, which does not produce significant reactions at beam ends opposite

302 an external load. This behavior gradually changes as we approach $a = 0.05$ but is clearly after the
303 experimental data at $a = 0.075$.
304



306

307 **Figure 5: Auxetic mechanical metamaterial.** A) Characteristic unit cell voxel demonstrating
 308 reentrant mechanism action resulting in negative transverse strain in response to compressive
 309 load, B) Experimental test setup for $n = 1-4$, undeformed (L), and deformed to 0.2 strain (R), with
 310 partial auxetic behavior visible, C) Simulation results recreating experiments, with out of plane
 311 reentrant behavior highlighted, D) Geometric parameters for simulations, where reentrant
 312 distance d is a function of lattice pitch P , E) Effective Poisson's ratio simulation and experimental
 313 results, F) 3D contour plot demonstrating effect of boundary conditions resulting in near zero
 314 Poisson's ratio at edges.

315

316
317
318
319
320
321
322
323
324
325
326
327
328
329
330
331
332
333
334
335
336
337
338
339
340
341
342
343
344
345
346
347
348
349

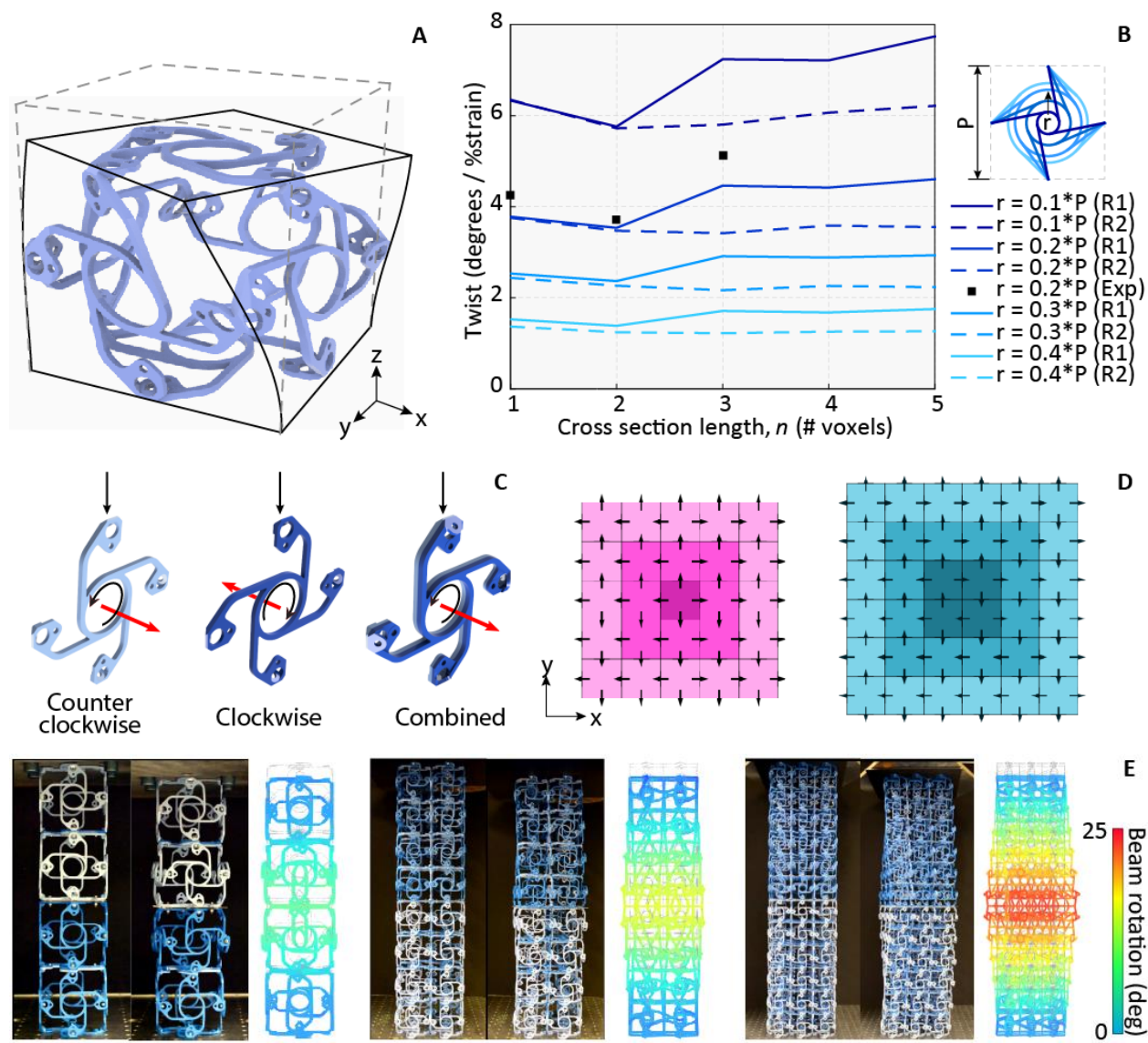
The goal of the auxetic lattice type is to exhibit a controllable negative Poisson's ratio. We present experimental and numerical results for the auxetic lattice type in Figure 5. The characteristic behavior of a unit cell voxel is shown in Figure 5A. Due to the internal architecture, which consists of interconnected, re-entrant mechanisms seen elsewhere in literature (14), the cell responds to axial strain with a similarly signed transverse strain, resulting in a negative Poisson's ratio ν , where $\nu = -\epsilon_{trans}/\epsilon_{axial}$. This value can be controlled based on the re-entrant distance d as a function of lattice pitch P , as shown in Figure 5D.

Experimental results are shown in Figure 5B. Lattice specimens are cubes of voxel width $n = 1-4$. Specimens were compressed to identical strain values ($\epsilon_{axial} = 0.2$), and transverse strain was measured by visually tracking points using fiducials mounted to the nodes along transverse faces (yz plane) parallel to the camera. Experimental data can be found in Figure S7-C. These results are slightly obscured due to reduced reentrant behavior at the edges of the lattice. In Figure 5C, we show contour plots element translation in the y direction, which is out of plane and normal to the camera view. While this behavior is generally isotropic, it should be noted that the effect of the internal mechanisms is reduced at the corners/edges of the cube specimen, as shown in Figure 5F. This effect is taken into account when calculating the effective strain values which are plotted in Figure 5E, over the range of parameters shown in Figure 5D.

There are two main insights from this study. First is that the effective metamaterial behavior approaches a nominal continuum value as cube side length of voxel count n increases. For any re-entrant distance, this behavior can be attributed to the increase of internal mechanism architecture relative to boundary conditions. Boundary conditions increase as a function of surface area proportional to n^2 , while internal mechanism architecture increases as a function of specimen volume proportional to n^3 . For lower values of d , the single voxel demonstrates lower values for Poisson's ratio (increased auxetic behavior) compared to multi-voxel specimens, but this is strongly influenced by boundary conditions, and should be considered an outlier.

The second insight is that the effective Poisson's ratio decreases (becomes more negative) as re-entrant distance d is increased, for voxel specimens larger than $n = 1$. This can be understood by considering the continuous beams of the re-entrant faces as a pseudo rigid body model (PRBM), where continuous flexural mechanisms are discretized as effectively rigid links connected by planar joints with torsional stiffness (ie: a spring) (31). As d decreases, so does link length, causing less clearly defined boundaries between the rigid link and compliant spring joint (see supplementary material for further analysis). As a result, the rigid link behavior begins to dominate, causing higher overall effective stiffness and lower compliance, thus reducing the re-

350 entrant mechanism efficacy. Further description of this behavior can be found in supplementary
351 material.
352



354

355

356 **Figure 6: Chiral mechanical metamaterial.** A) Characteristic unit cell voxel demonstrating out
 357 of plane coordinated rotation in response to compressive load, B) Simulation and experimental
 358 results for odd and even column cross sections in combination with design rules 1 and 2, C) Two
 359 chiral part types allow internal frustration to be avoided, thus enabling scalable chiral
 360 architecture, D) Design rules 1 (L) and 2 (R), which emerge from odd and even columns,
 361 respectively, E) Experimental and simulation results of $n = 1, 2,$ and $3,$ showing total twist
 362 increases as column voxel width increases, but normalized twist per strain is lower for $n = 2.$

363

364 The chiral lattice type exhibits scalable twisting behavior, which is attributable to having
365 two chiral part types, and developing a construction logic to avoid internal frustrations. We
366 present experimental and numerical results for the chiral lattice type in Figure 6. The
367 characteristic behavior of a unit cell voxel is shown in Figure 6A. Based on the chirality
368 orientation, the cell will respond to an axial strain with a macroscopic twisting in either the CW or
369 CCW direction, in the plane normal to the direction of loading (ie: loading in z direction results in
370 twisting in xy plane). The effective chirality can be measured as degrees twist per unit strain.

371 Experimental results are shown next to their numerical simulations in Figure 6E. Lattice
372 specimens are designed as columns with 1:4 width to height ratio, similar to (15). The top half is
373 CCW chiral lattice and the bottom half is CW chiral lattice. This produces the largest net twist at
374 the rigid interface between the two halves and allows fixed boundary conditions at the top and
375 bottom. Chiral columns of 1x1x4, 2x2x8, and 3x3x12 were tested in compression to identical
376 strain values ($\epsilon_{axial} = 0.05$), and twist was measured by tracking a single point at the center of
377 the lattice. Experimental results are shown in Figure S7-D. Surprisingly, the 1x1x4 shows larger
378 values for twist than the 2x2x8. This is attributable to internal architecture, which is also the cause
379 of the scalable twisting found over a range of beam sizes.

380 Experimental values for twist per strain are shown next to simulation results in Figure 6B,
381 over a range of values for radius r of the face part as a function of lattice pitch P , with increasing
382 column voxel width n . We observe an increase twist per strain for smaller values of r . This is
383 attributable to the direct relationship between strain and twist as a function of the rotational
384 mechanism. If we assume a unit strain is translated into an arc length s , then the rotation angle θ
385 increases as circle radius r goes to zero, given $\theta = s/r$. However, given a nominal beam
386 thickness t , there is a limit to how small r can become before the mechanism becomes ineffective.
387 See supplementary material for further analysis.

388 There are several key takeaways from this. First, we see that performance does not
389 decrease monotonically with increasing voxel count n , but rather stabilizes to a continuum value.
390 This is in contrast to comparable results in literature (15), and can be explained by looking more
391 closely at the combination of CW and CCW part types. Done properly, internal frustrations—
392 when CW and CCW faces are joined they essentially cancel each other's twist, resulting in zero
393 twist per strain—can be avoided, as shown in (32) by using voids. In our case, we get improved
394 twist performance by logically designing the internal architecture according to rules chosen to
395 avoid frustration. This means that voxel types are directionally anisotropic, in contrast to the
396 previous three lattice types, and further are spatially programmed to produce desired global
397 effective behavior. Strategies for this spatial programming are shown in Figure 6C. On the left,

398 we show a beam with odd number voxel widths. Here, design rule #1 is to orient the net face
399 chirality (represented as arrows) away from the column interior. The experimental lattices for $n=1$
400 and $n=3$ widths were built using rule #1. Design rule #2 was developed starting from $n=2$, where
401 the orientation of interior faces is ambiguous when following rule #1. Rule #2 introduces
402 continuous, clockwise circumferential orientation of the interior chiral faces and was used in
403 construction the $n=2$ experimental articles. Both rules are hierarchical, e.g. a rule #1 5×5 column
404 contains a 3×3 and 1×1 column in its interior as shown in Figure 6C. Simulations were performed
405 for all column widths using both rules and show decreased twist response for rule #2, in
406 agreement with experimental measurements. These rules were determined empirically and are not
407 considered exhaustive but indicate the importance of rational design in this lattice type.
408

409 Discussion

410 In this paper, we presented a method for producing large scale mechanical metamaterials
411 through discrete assembly of modular, mass-produced parts. We showed that bulk, continuum
412 behavior can be achieved through design of the parts and connections, ensuring global behaviors
413 are governed by local properties. We presented a finite set of part types which exhibit a diverse
414 range of behaviors. Rigid lattice types show linear stiffness to density scaling with predictable
415 failure modes. Compliant lattice types show quadratic stiffness to density scaling, as well as
416 unique bulk behavior at low cell count, such as near-zero Poisson's ratio. Auxetic lattice types
417 show controllable, isotropic negative Poisson's ratio. Chiral lattice types show scalable transverse
418 twist in response to axial strain, which is a result of two part types being used to prevent internal
419 architectural frustration. All four part types showed good agreement with numerical results, and
420 their behavior is predictable through analytical means. All lattice types are made the same way:
421 parts are injection molded and assembled with blind rivets to make voxels, and voxels are
422 similarly joined to build lattice. This is a low cost, highly repeatable process that promises to
423 enable mechanical metamaterials at macro scales (Figure S8).

424 There are several constraints of the current system which are important to consider for
425 scalability and performance. This approach is based on discrete assembly of mass-produced parts,
426 and there are inherent constraints for both part production and assembly. While discrete lattice
427 assembly as a method is material-agnostic, our current part production method is limited to
428 materials that can be injection molded. This includes elastomers, polymers, and various fiber
429 composites, but generally excludes ceramics, metals, and natural materials. However, there are
430 numerous digital fabrication processes with sufficient precision, repeatability, and throughput to
431 make parts for discrete lattice assembly. Metal parts can be produced with low cost, highly
432 repeatable processes such as stamping or laser cutting, the latter having been previously
433 demonstrated (33). Ceramic parts can be cast in batches, though firing or curing time may
434 produce a bottleneck. Parts made from natural materials such as wood can be made with
435 subtractive laser cutting or milling, the latter providing the option for true 2.5D or full 3D
436 geometric feature capabilities. Concerns here include material waste as well as undesired
437 anisotropy of the stock material from which parts are made.

438 Once parts are produced, they need to be joined. The appeal of using mechanical fasteners
439 is high structural efficiency, good repeatability, and the potential for reversibility. However,
440 parasitic joint mass is also a consequence. Both node and fastener mass are considered parasitic
441 due to the effective lattice behavior being governed by beam properties, as described previously.
442 While this effectively makes the joints disappear structurally, their mass is still included in

443 calculating lattice mass and density. Therefore, joints should be as small as possible while still
444 achieving the needed mechanical performance to ensure proper lattice behavior. This is an
445 inherent tradeoff of discrete assembly. The other constraint is related to scale. As global lattice
446 scale reduces from meters to centimeters and millimeters, joints become difficult to realize with
447 COTS fasteners and may require more customized solutions. In addition, at these scales, it is
448 possible to manufacture comparable lattice with aforementioned additive processes. At small
449 scales, the benefits of additive manufacturing can outweigh the benefits of discrete assembly and
450 should be considered against cost and performance criteria.

451 Full-scale applications typically require additional steps for implementation, including
452 interfaces with more traditional hardware systems as well as external stimuli. For example, in
453 Figure S9, we show an experimental ground vehicle made with the rigid discrete lattice presented
454 here. The lattice structures discussed here are open cell, which enables great sparsity and low
455 density. Partial or closed surfaces may be desired to receive hydro or aerodynamic pressures. For
456 example, discrete lattices have been demonstrated previously as lightweight, morphing
457 aerostructures. Skins, or outer mold lines, are achieved with discrete strips (34) or panels (35). In
458 both cases, the discrete nature of the skin is designed to mirror that of the lattice, both in
459 geometric pitch and characteristic length. Structurally, these skins must transfer pressure loads to
460 the lattice and not deform plastically or fail in tension, but they do not act as a traditional
461 monocoque structure, thus allowing them to be discretized. Skin material and thickness is then
462 informed by these constraints, while seeking to minimize mass. Alternatively, in higher
463 magnitude loading scenarios, more robust panels provide significant factors of safety, such as
464 providing a walking surface on a 5m lattice bridge (26). In this case, a total of nine panels
465 weighed roughly 10kg, while the lattice, made up of 156 voxels, weighed roughly 18kg. Thus,
466 skin or surface elements can contribute significant mass and must be considered if the application
467 is mass-critical, as many aerospace applications are.

468 While manual assembly has sufficiently high throughput for lab-based experiments (see
469 Table S1), full-scale implementations with voxel counts over 10^2 will benefit greatly from
470 automation. Stationary gantry platforms have been fitted with end effectors for voxel transport
471 and bolting operations (36), and mobile robots have been implemented to perform similar
472 operations while locomoting on the lattice as they construct it (37). Stationary systems promise
473 high throughput for a bounded work envelope, while mobile robots can be parallelized and
474 require no global positioning due to local alignment features, offering benefits of autonomy and
475 reliability. Automation will be critical for producing these metamaterials and structures in large
476 quantities envisioned for commercial applications.

477 Finally, the scope of this paper is limited to homogeneous lattice types (subtleties of chiral
478 architecture aside). Due to the consistent assembly method across part types, heterogeneous
479 lattices can be made with this approach just as easily. Heterogeneous metamaterials have been
480 shown to have exponential combinatorial possibilities (38), as well as the ability to realize any
481 arbitrary elasticity tensor (39). Next steps for this work include harnessing spatial programming to
482 achieve diverse anisotropy with simple design rules applied to our finite set of parts.

483 By offering a simple yet diverse set of parts unified with a consistent assembly method,
484 this work represents a significant step in lowering the barrier for entry to realizing the promise of
485 metamaterials. Combined with hierarchical design tools and assembly automation, we foresee this
486 research enabling emerging fields such as soft robotics, responsive aero and hydrodynamic
487 structures, and user-defined programmable materials, thereby further merging the digital and
488 physical sides of future engineering systems.

489

490

Materials and Methods

Injection molding and assembly: Part production and assembly details are shown in Figure S1. Parts were injection molded by Protolabs, a US-based CNC manufacturing service provider. To ensure low cost, parts were designed to be two-part moldable. While this is simple for the majority of the part, the inner-voxel tab and hole at 45 degrees required a custom designed opening, shown in Figure S1C. Parts were assembled with 3/32" diameter blind aluminum rivets, utilizing a pneumatic rivet gun. The voxel assembly process is shown in Figure S1D. Voxel to voxel joints used the same process, shown in Figure S1E. Metrics for assembly time and throughput are shown in Table S1.

Mechanical characterization: Small-scale tests to validate continuum behavior as shown in Figure 1 were performed on an Instron 4411 testing machine using a 5kN load cell. Lattice specimens for each type were tested in cubes of side length voxel count $n = 1, 2, 3,$ and 4. Lattice tests were performed on an Instron 5985 testing machine using a 250 kN load cell. Specimens of a given lattice type were loaded to the same amount of relative strain, at an extension rate of 10 mm/min. Both machines use Bluehill 2 software for data acquisition. Video was recorded using a Nikon D3400 camera. Video was analyzed using Tracker, an open source video analysis and modeling tool (<https://physlets.org/tracker/>).

Numerical modeling: Fully meshed FEA simulations were used to check stress concentrations, but these typically incur higher computational costs (Figures S5-6), and therefore were limited to under 10 voxels. A static stress analysis solver based on NASTRAN was used in Autodesk Fusion 360's built in simulation environment. Larger lattice models were simulated using the Frame3DD library, a freely available numerical solver implementing Timoshenko beam elements (<http://frame3dd.sourceforge.net/>) along with a python interface, PyFrame3DD (<https://github.com/WISDEM/pyFrame3DD>). For analysis of asymptotic behavior of large lattices Frame3DD was modified to incorporate sparse matrix math using CHOLMOD from the SuiteSparse library (<https://github.com/DrTimothyAldenDavis/SuiteSparse>). Python utilities were written to automate creating nodes, edges, faces and voxels, as well as applying loadings and boundary conditions using spatial rules (e.g. fixing the bottom of a lattice and applying forcing to the top nodes). These simulations were validated against a commercial software with comparable sparse matrix solving capabilities (Oasys GSA v9.0).

525 **Acknowledgements**

526 **Funding:** This work was supported by: NASA Cooperative Agreement
527 #80NSSC19M0039, US Army Research Lab Cooperative Agreement #W911NF1920117, and
528 CBA Consortia funding.

529 **Author Contributions:** BJ designed and produced parts, CC developed code to perform
530 sparse matrix numerical modeling, FT performed numerical modeling using best-practice
531 commercial packages, AP performed mechanical testing of lattice and subsystems, MO led lattice
532 test specimen assembly, NG provided system architecture guidance.

533 **Competing interests:** the authors cite no competing interests.
534

535 **References**

- 536 1. L. Gibson, *Cellular Solids: Structure and Properties* (Cambridge University Press, 1999).
- 537 2. R. Lakes, Materials with structure hierarchy. *Nature*. **361**, 511–515 (1993).
- 538 3. L. J. Gibson, M. F. Ashby, The Mechanics of Three-Dimensional Cellular Materials. *Proc.*
539 *R. Soc. A Math. Phys. Eng. Sci.* (2006), doi:10.1098/rspa.1982.0088.
- 540 4. M. F. Ashby, The properties of foams and lattices. *Philos. Trans. A. Math. Phys. Eng. Sci.*
541 **364**, 15–30 (2006).
- 542 5. V. S. Deshpande, M. F. Ashby, N. a. Fleck, Foam topology: Bending versus stretching
543 dominated architectures. *Acta Mater.* **49**, 1035–1040 (2001).
- 544 6. T. A. Schaedler, A. J. Jacobsen, A. Torrents, A. E. Sorensen, J. Lian, J. R. Greer, L.
545 Valdevit, W. B. Carter, Ultralight metallic microlattices. *Science (80-.)*. **334**, 962–965
546 (2011).
- 547 7. X. Zheng, H. Lee, T. H. Weisgraber, M. Shusteff, J. DeOtte, E. B. Duoss, J. D. Kuntz, M.
548 M. Biener, Q. Ge, J. a Jackson, S. O. Kucheyev, N. X. Fang, C. M. Spadaccini, Ultralight,
549 ultrastiff mechanical metamaterials. *Science*. **344**, 1373–7 (2014).
- 550 8. X. Zheng, W. Smith, J. Jackson, B. Moran, H. Cui, D. Chen, J. Ye, N. Fang, N. Rodriguez,
551 T. Weisgraber, C. M. Spadaccini, Multiscale metallic metamaterials. *Nat. Mater.* (2016),
552 doi:10.1038/nmat4694.
- 553 9. L. R. Meza, S. Das, J. R. Greer, Strong , Lightweight and Recoverable Three -
554 Dimensional Ceramic Nanolattices. *Submitted*. **345**, 1322–1326 (2014).
- 555 10. J. B. Berger, H. N. G. Wadley, R. M. McMeeking, Mechanical metamaterials at the
556 theoretical limit of isotropic elastic stiffness. *Nature*. **543**, 533–537 (2017).
- 557 11. L. A. Shaw, F. Sun, C. M. Portela, R. I. Barranco, J. R. Greer, J. B. Hopkins,
558 Computationally efficient design of directionally compliant metamaterials. *Nat. Commun.*
559 (2019), doi:10.1038/s41467-018-08049-1.
- 560 12. Y. Jiang, Q. Wang, Highly-stretchable 3D-architected Mechanical Metamaterials. *Sci. Rep.*
561 (2016), doi:10.1038/srep34147.
- 562 13. X. Ren, R. Das, P. Tran, T. D. Ngo, Y. M. Xie, Auxetic metamaterials and structures: A
563 review. *Smart Mater. Struct.* (2018), , doi:10.1088/1361-665X/aaa61c.

- 564 14. F. Wang, Systematic design of 3D auxetic lattice materials with programmable Poisson's
565 ratio for finite strains. *J. Mech. Phys. Solids* (2018), doi:10.1016/j.jmps.2018.01.013.
- 566 15. T. Frenzel, M. Kadic, M. Wegener, Three-dimensional mechanical metamaterials with a
567 twist. *Science* (80-.). (2017), doi:10.1126/science.aao4640.
- 568 16. T. A. Schaedler, W. B. Carter, Architected Cellular Materials. *Annu. Rev. Mater. Res.* **46**,
569 187–210 (2016).
- 570 17. A. R. Torrado, D. A. Roberson, Failure Analysis and Anisotropy Evaluation of 3D-Printed
571 Tensile Test Specimens of Different Geometries and Print Raster Patterns. *J. Fail. Anal.*
572 *Prev.* (2016), doi:10.1007/s11668-016-0067-4.
- 573 18. L. Bochmann, C. Bayley, M. Helu, R. Transchel, K. Wegener, D. Dornfeld, Understanding
574 error generation in fused deposition modeling. *Surf. Topogr. Metrol. Prop.* (2015),
575 doi:10.1088/2051-672X/3/1/014002.
- 576 19. L. Liu, P. Kamm, F. García-Moreno, J. Banhart, D. Pasini, Elastic and failure response of
577 imperfect three-dimensional metallic lattices: the role of geometric defects induced by
578 Selective Laser Melting. *J. Mech. Phys. Solids* (2017), doi:10.1016/j.jmps.2017.07.003.
- 579 20. C. E. Duty, V. Kunc, B. Compton, B. Post, D. Erdman, R. Smith, R. Lind, P. Lloyd, L.
580 Love, Structure and mechanical behavior of Big Area Additive Manufacturing (BAAM)
581 materials. *Rapid Prototyp. J.* **23**, 181–189 (2017).
- 582 21. B. Khoshnevis, D. Hwang, K.-T. Yao, Z. Yah, Mega-scale fabrication by contour crafting.
583 *Int. J. Ind. Syst. Eng.* (2006), doi:10.1504/IJISE.2006.009791.
- 584 22. X. Zhang, et al, Large-scale 3D printing by a team of mobile robots. *Autom. Constr.*
585 (2018).
- 586 23. Nanoscribe GmbH, Nanoscribe Technology. *nanoscribe.de/en/technology/* (2017).
- 587 24. Masterprint, (available at [https://en.machinetools.camozzi.com/products/additive-](https://en.machinetools.camozzi.com/products/additive-manufacturing/all-products/masterprint.kl)
588 [manufacturing/all-products/masterprint.kl](https://en.machinetools.camozzi.com/products/additive-manufacturing/all-products/masterprint.kl)).
- 589 25. K. C. Cheung, N. Gershenfeld, Reversibly assembled cellular composite materials. *Science*.
590 **341**, 1219–21 (2013).
- 591 26. B. Jenett, D. Cellucci, C. Gregg, K. C. Cheung, in *Proceedings of the 2016 Manufacturing*
592 *Science and Engineering Conference* (2016).

- 593 27. C. Gregg, J. Kim, K. Cheung, Ultra-Light and Scalable Composite Lattice Materials. *Adv.*
594 *Eng. Mater.* (2018), doi:<https://doi.org/10.1002/adem.201800213>.
- 595 28. W. Chen, S. Watts, J. A. Jackson, W. L. Smith, D. A. Tortorelli, C. M. Spadaccini, Stiff
596 isotropic lattices beyond the Maxwell criterion. *Sci. Adv.* (2019),
597 doi:10.1126/sciadv.aaw1937.
- 598 29. N. Wang, Z. Zhang, X. Zhang, Stiffness analysis of corrugated flexure beam using stiffness
599 matrix method. *Proc. Inst. Mech. Eng. Part C J. Mech. Eng. Sci.* (2019),
600 doi:10.1177/0954406218772002.
- 601 30. V. Goga, in *Computational Methods in Applied Sciences* (2011).
- 602 31. L. L. Howell, S. P. Magleby, B. M. Olsen, *Handbook of Compliant Mechanisms* (2013).
- 603 32. P. Ziemke, T. Frenzel, M. Wegener, P. Gumbsch, Tailoring the characteristic length scale
604 of 3D chiral mechanical metamaterials. *Extrem. Mech. Lett.* (2019),
605 doi:10.1016/j.eml.2019.100553.
- 606 33. B. Jenett, N. Gershenfeld, P. Guerrier, in *ASME MSEC* (2018).
- 607 34. B. Jenett, S. Calisch, D. Cellucci, N. Cramer, N. Gershenfeld, S. Swei, K. C. Cheung,
608 Digital Morphing Wing: Active Wing Shaping Concept Using Composite Lattice-Based
609 Cellular Structures. *Soft Robot.* **4** (2017), doi:10.1089/soro.2016.0032.
- 610 35. N. Cramer, D. Cellucci, O. Formoso, C. Gregg, B. Jenett, J. Kim, M. Lendraitis, S. S. Swei,
611 K. Trinh, G. Trinh, K. Cheung, Elastic Shape Morphing of Ultralight Structures by
612 Programmable Assembly. *Smart Mater. Struct.* (2019).
- 613 36. G. Trinh, D. Cellucci, B. Jenett, S. Nowak, S. Hu, M. O'Connor, G. Copplestone, K.
614 Cheung, in *IEEE Aerospace Conference Proceedings* (2017).
- 615 37. B. Jenett, A. Abdel-Rahman, K. C. Cheung, N. Gershenfeld, Material-Robot System for
616 Assembly of Discrete Cellular Structures. *IEEE Robot. Autom. Lett.* (2019), doi:doi:
617 10.1109/LRA.2019.2930486.
- 618 38. C. Coullais, E. Teomy, K. De Reus, Y. Shokef, M. Van Hecke, Combinatorial design of
619 textured mechanical metamaterials. *Nature* (2016), doi:10.1038/nature18960.
- 620 39. G. W. Milton, A. V. Cherkaev, Which elasticity tensors are realizable? *J. Eng. Mater.*
621 *Technol. Trans. ASME* (1995), doi:10.1115/1.2804743.

622 40. W. C. Young, R. G. Budynas, Roark's Formulas for Stress and Strain. *Library (Lond)*. **7**,
623 832 (2002).

624

625

1 **Supplementary Materials**

2 Figure S 1: Production of lattice by injection molding and assembly.

3 Figure S 2: Load paths in rigid Cuboct lattice.

4 Figure S 3: Relationship between compression member slenderness ratio, failure mode, and
5 resulting lattice relative density.

6 Figure S 4: Free body diagram of unit cell for each lattice type.

7 Figure S 5: Comparison of numerical models for a single rigid cuboct voxel.

8 Figure S 6: Comparison of numerical modeling methods and results.

9 Figure S 7: Experimental results.

10 Figure S 8: As-built lattice specimens.

11 Figure S 9: Large scale application of discretely assembled mechanical metamaterial as a car
12 frame.

13 Table S 1: Assembly metrics

14

15 Video files:

16 Video S1: Rigid lattice type

17 Video S2: Compliant lattice type

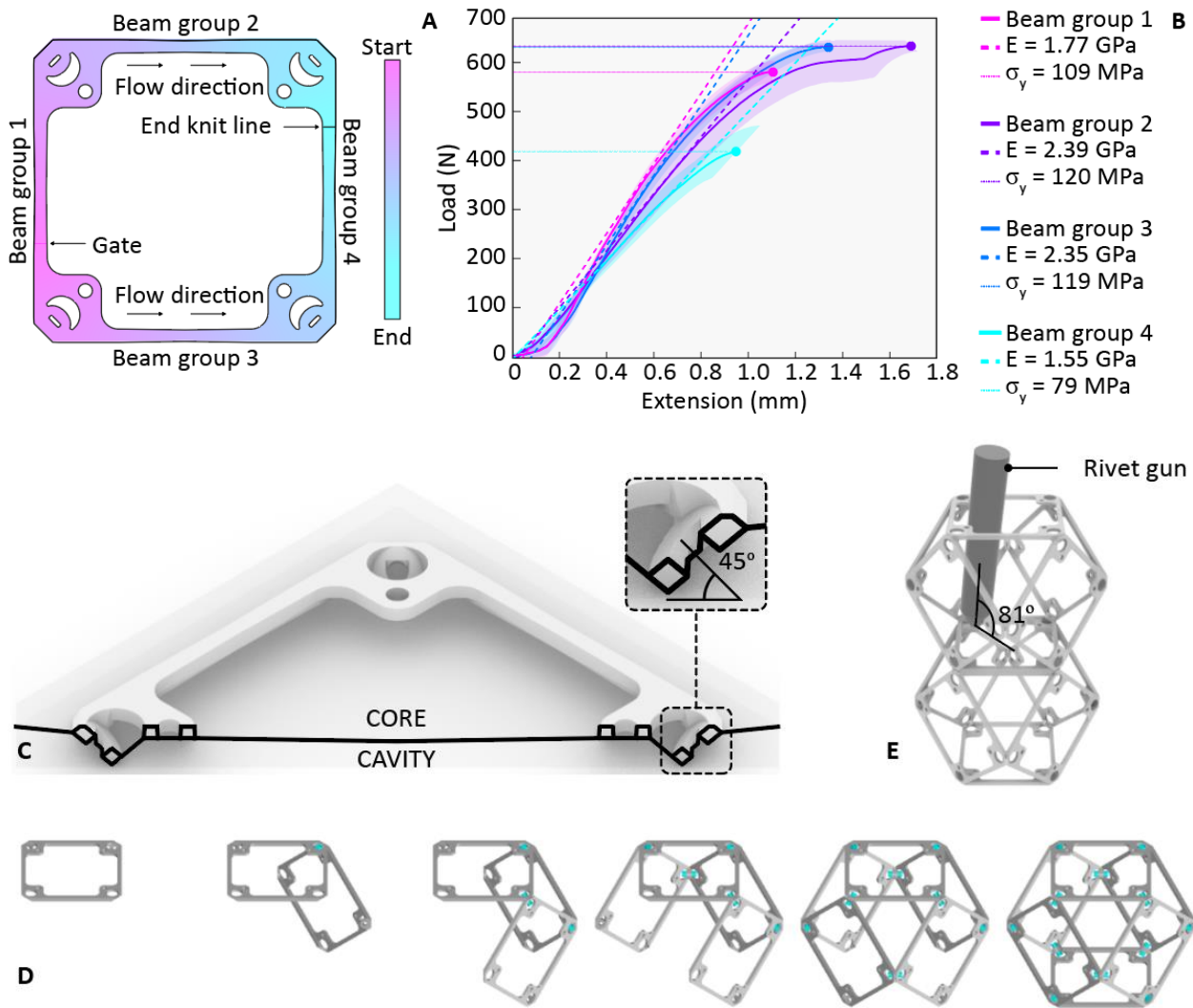
18 Video S3: Auxetic lattice type

19 Video S4: Chiral lattice type

20

21

22 **Part geometry, molding, assembly**



23

24

25 **Figure S 1: Production of lattice by injection molding and assembly.** A) Injection molding gate
 26 layout and resulting material flow and knit line location, B) Characterization of different beam
 27 groups based on relative locations on part, C) Two part mold, with cavity below and core above,
 28 and a detailed view of the 45 degree angle hole, which is achieved by splitting the feature
 29 between core and cavity, D) Voxel assembly sequence. Faces are joined together one at a time,
 30 using rivets at the corners. A voxel consists of six faces and twelve rivets. E) Neighboring voxels
 31 are joined with the same method, rivet gun shown entering opposite face, at slight angle due to
 32 interference with inter-voxel joint node of entering face.

33

34 We characterized the as-molded properties of the GFRP material, where the elastic
35 modulus and yield strength vary based on the location of the gate and resulting knit lines. For
36 injection molded FRP, fiber concentration reduces with distance from the gate. The highest
37 concentration is around the gate, resulting in relatively high stiffness, but residual thermal and
38 mechanical stress from the injection process cause a relatively lower yield strength. At the end of
39 the flow, knit lines can result in around 50% yield strength reduction (27), in addition to reduced
40 elastic modulus owing to distance from the gate. Therefore, controlling the location of these
41 features is important. We want to avoid having the gate or knit line occur near the middle of the
42 beam, where stress will be magnified during beam buckling induced strain. We also want to avoid
43 having the end knit line occur on the inter- or inner-voxel nodes. Aside from operational stresses,
44 during the voxel construction the outward force of the rivet expanding from actuation causes
45 circumferential stress in the node area which can result in rupture along knit lines.

46 The resulting gate and knit line locations are shown for the rigid part type in Figure S1A,
47 with contours indicating the flow location at increasing time steps. To characterize the range of
48 as-molded material properties, specimens from each beam group were extracted from the faces
49 and tested in uniaxial tension until failure, and the resulting elastic modulus and yield strength
50 were calculated, as shown in Figure S1B. Our findings confirm several key aspects of part
51 production. Beam group 1, which is closest to the gate, has high fiber content, thus a high elastic
52 modulus, but has lower yield strength due to residual stress caused by gate proximity. Beam
53 groups 2 and 3 have flows that move continuously from one end to the other, which promotes
54 axial fiber alignment, giving a higher elastic modulus and yield strength. The last beam group has
55 the lowest modulus, due to being at the end of the flow front, and the lowest strength, due to knit
56 line proximity.

57

58

59

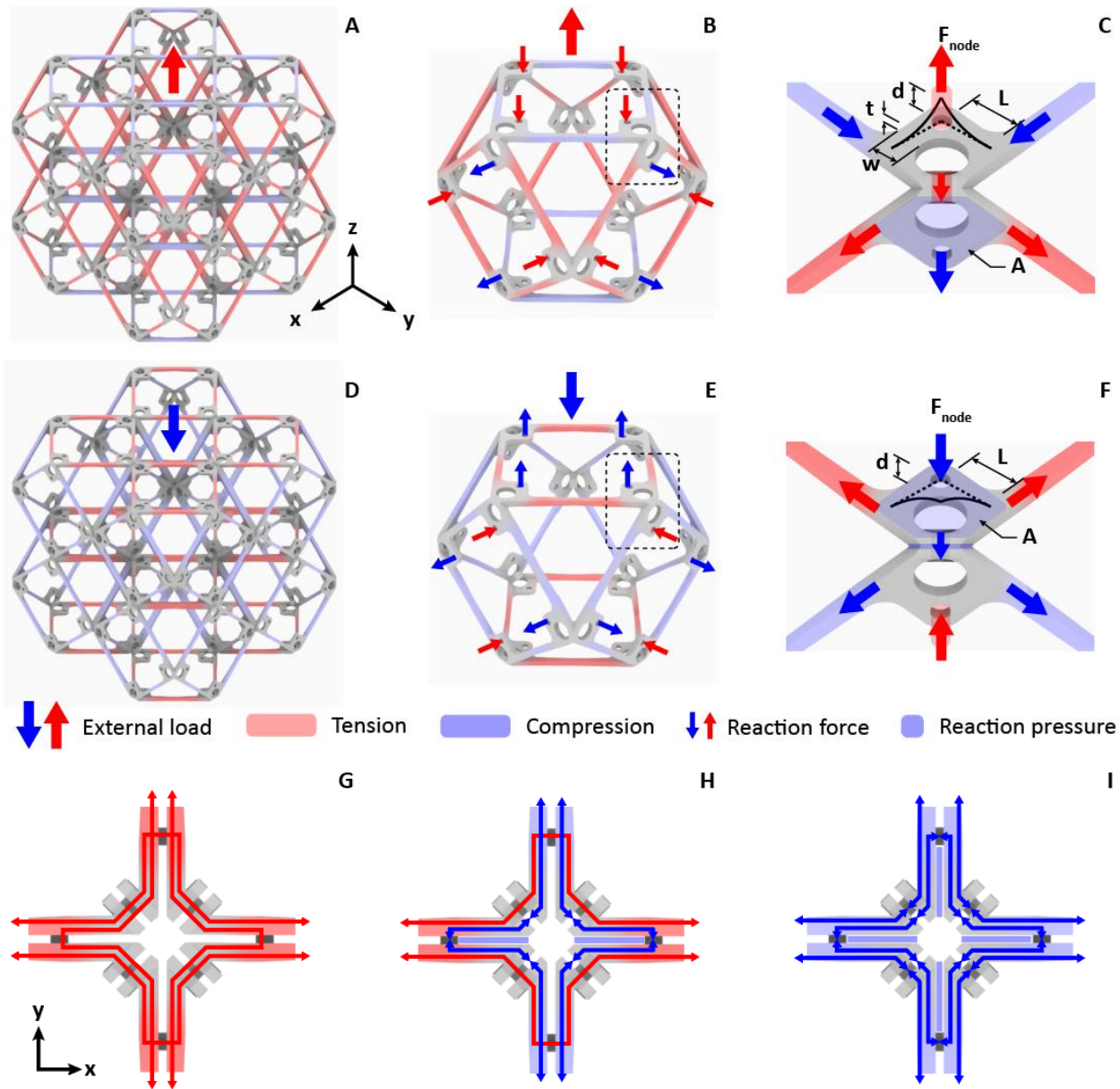
60

61

62

63 **Discrete lattice load path analysis**

64



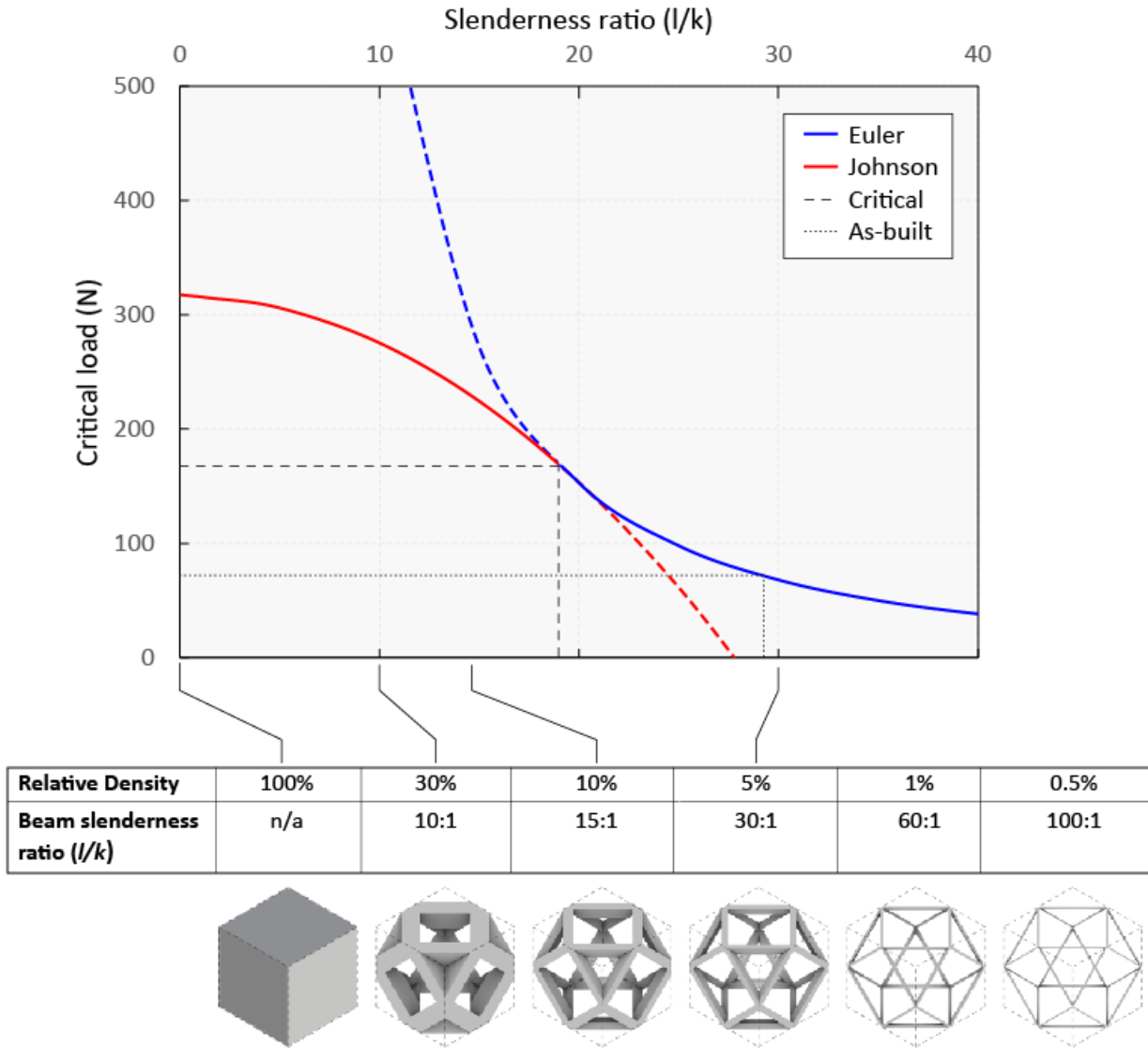
67 **Figure S 2: Load paths in rigid Cuboct lattice.** A) $2 \times 2 \times 2$ cube under uniaxial tension in Z
 68 direction, B) sample voxel under tension in Z direction, C) detail of corner joint showing internal
 69 load transfer, D) $2 \times 2 \times 2$ cube under uniaxial compression in Z direction, E) sample voxel under
 70 compression in Z direction, F) detail of corner joint showing internal load transfer, G)
 71 illustration of cross-axis load transfer at joints, showing XZ and YZ planes in uniform tension, H)
 72 mixed compression and tension, and I) uniform compression.

73

74 The rigid cuboct is taken as the “base” unit, which is used for describing system architecture
75 such as critical dimensions and relative structural performance metrics. Figure S2A shows a
76 2x2x2 cube loaded in tension in the positive Z direction. We can observe that in-plane beams
77 parallel to the loading direction (XY and YZ planes) go into tension, which results in the out of
78 plane members (XY plane) go into compression. Assuming periodic boundary conditions, a single
79 representative voxel is shown in Figure S2B, where external loading and reaction forces at
80 outward facing nodes are shown. XY plane nodes logically go into tension on the top and bottom
81 faces of the voxel. XZ and YZ faces have combined tension and compression reaction forces at
82 the nodes, while all beams are in tension. Due to the construction employed, in-plane face loads
83 are transferred through adjacent nodes to the outward face, which is normal to the load path
84 direction, as shown in Figure S2C. At the junction of four, in-plane voxels, there are 3 possible
85 load paths: all compression, all tension, or mixed tension and compression (Figure S2G-I). All
86 compression is resolved through contact pressure of the node area, which helps in reducing the
87 resulting pressure magnitude. All tension loads transfer from in plane beams, through inner-voxel
88 joints, then through rivets which are parallel to the load path but fixtured to faces which are
89 normal to the load path. Combined loads have overlapping, orthogonal load paths.

90

91 **Beam slenderness and relative density**



92

93 **Figure S 3: Relationship between compression member slenderness ratio, failure mode, and**
 94 **resulting lattice relative density.** Beams above the critical slenderness ratio ($l/k = 29.5$) fail by
 95 elastic buckling, beams below fail by plastic buckling. Relative densities above 30% are invalid
 96 for cellular theory to apply.

97 Here we discuss yield strength as the point at which initial beam failure occurs. The
 98 mechanism for this failure is important for understanding how the discrete lattice system behaves
 99 as a continuum lattice. As shown in Figure S 2, external loads are resolved internally as beam
 100 tension and compression. Beam tensile failure is determined by constituent material and beam
 101 cross sectional area, with the critical force $F_{cr} = \sigma_t * A$.

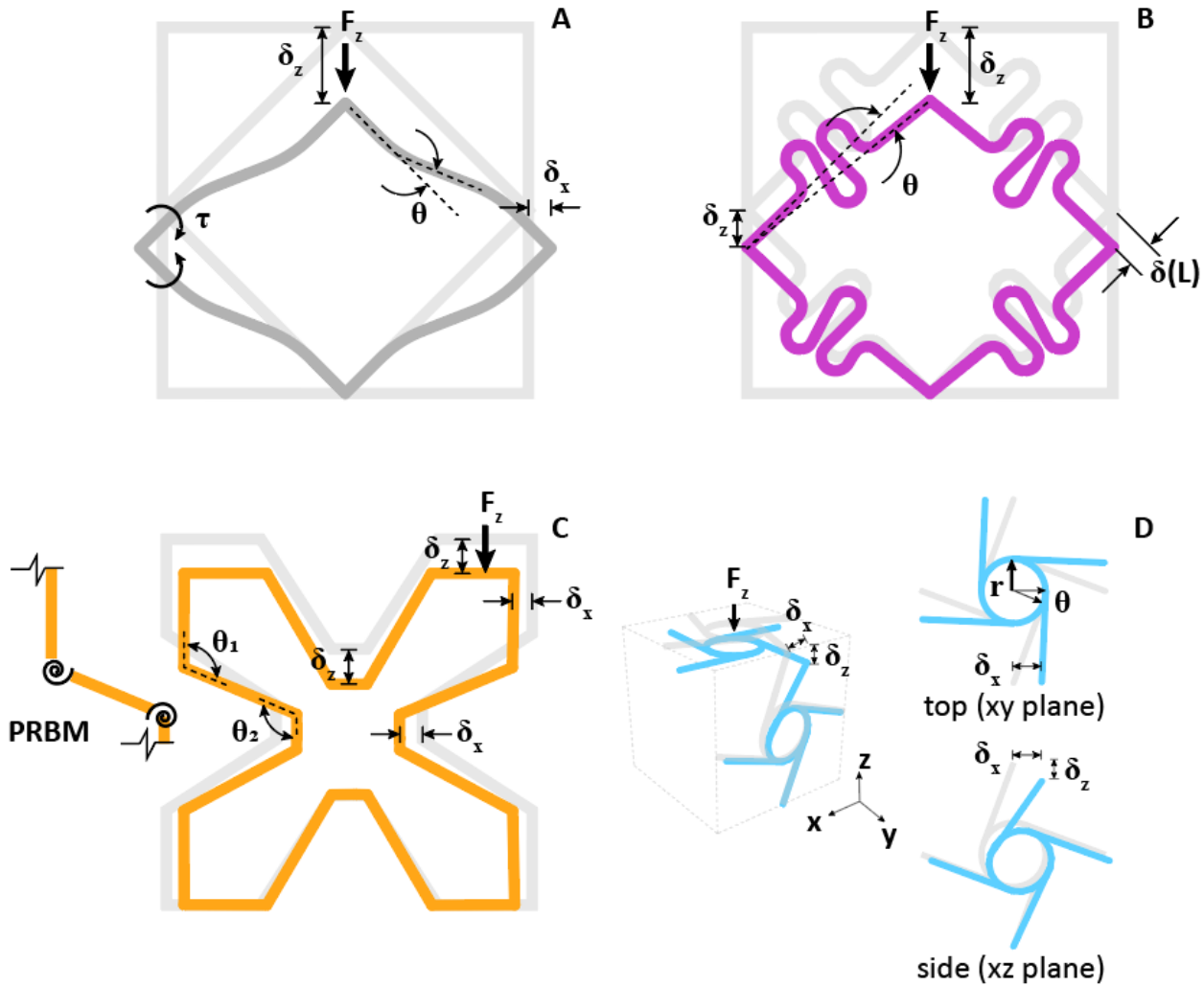
102 Beams in compression fail in different ways depending on their slenderness ratio, defined
 103 as effective length over radius of gyration, $(l/k) = L_{ef} \sqrt{A/I}$. This is used to describe three

104 compression member types in terms of their failure modes: short, intermediate, and long. As
105 cellular solid theory is only applicable at relative densities under 30%, we limit our analysis to
106 beams with slenderness ratios above 4:1 (see Figure S 3). For sparse Euler buckling is the elastic
107 stability limit, and is applicable to long members, but as slenderness ratio goes to zero, Euler
108 buckling predictions go to infinity. Therefore, the Johnson parabola curve considers material yield
109 strain (σ_y/E), the strain at which the material ceases to be linearly elastic [30], in calculating the
110 inelastic stability limit. The transition between long and intermediate occurs at the critical
111 slenderness ratio, which can be calculated using material and beam geometric properties (40).

112 Our material is a GFRP with an elastic modulus $E = 2$ GPa and yield strength $\sigma_y = 107$
113 MPa, and we can calculate critical slenderness using $(l/k)_{cr} = \sqrt{2\pi^2 E/\sigma_y} = 19.21$. Based on our
114 part geometry, we find our beam slenderness to be ~ 29.5 . Therefore, our beams should fail based
115 on Euler buckling at a critical load $F_{cr} = 70$ N. Using the yield strength values from Figure S 7A,
116 we can determine the experimental value for critical beam load by dividing the global peak load
117 (7.8 kN) by the cross sectional voxel count (16), resulting in 487.5 N/voxel, 121.9 N/node, which
118 is carried by two beams at 45 degree angles, giving a beam load of 86N.

119

120 Free body diagrams of each lattice type

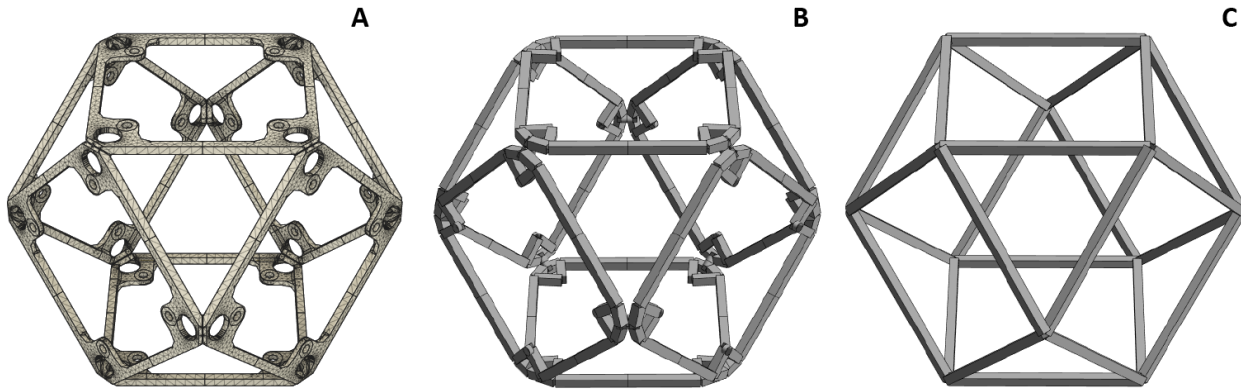


121

122 **Figure S 4: Free body diagram of unit cell for each lattice type.** A) Rigid lattice type resolves
 123 external loads through axial member forces, in this case shown as compression and resulting
 124 member buckling, B) Compliant lattice type resolves external loads through axial shortening
 125 combined with a small amount of bending, producing little to no lateral reaction forces at nodes,
 126 C) Auxetic lattice type deforms through bending at the joints, and can be considered a pseudo
 127 rigid body model as shown to the side, D) Chiral lattice type deforms by bending and rotation in
 128 side faces, and nearly pure rotation in top face, thus producing chiral response.

129

130 **Numerical Modeling Comparison**

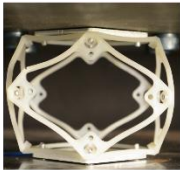
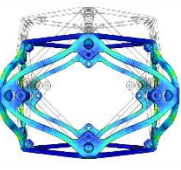
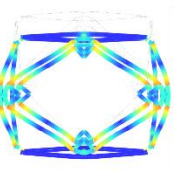
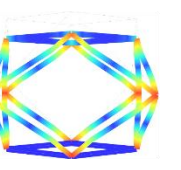
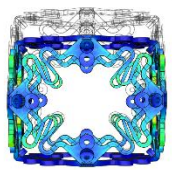
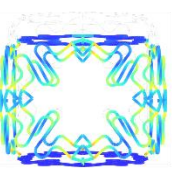
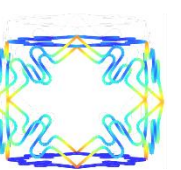
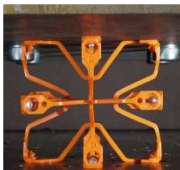
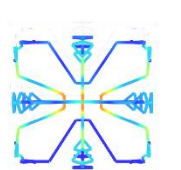
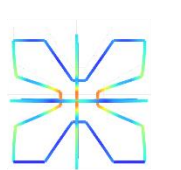
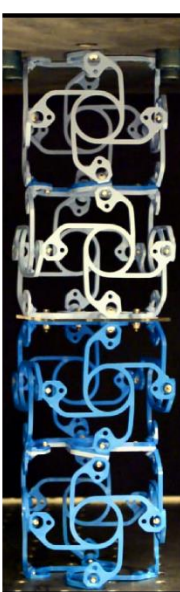
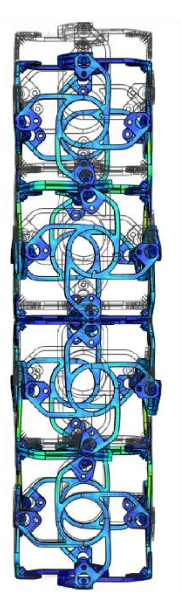
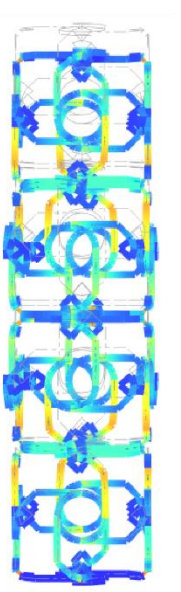
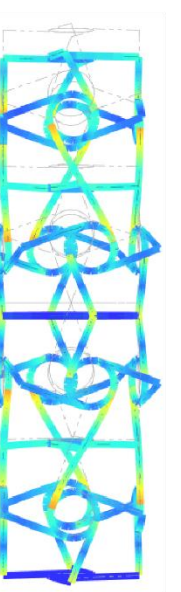


Nodes:	83,357	156	12
Elements:	44,500	192	24
DoF:	277,788	936	72

131

132 **Figure S 5: Comparison of numerical models for a single rigid cuboct voxel.** A) NASTRAN
133 (built in FEA for commercial CAD/CAE software, Autodesk Fusion), B) Beam model with
134 additional model detail of joints, C) Theoretical beam model.

135

Type	Experiment	FEA (NASTRAN)	Beam (as-built)	Beam (theory)
Rigid				
Compliant				
Auxetic				
Chiral				

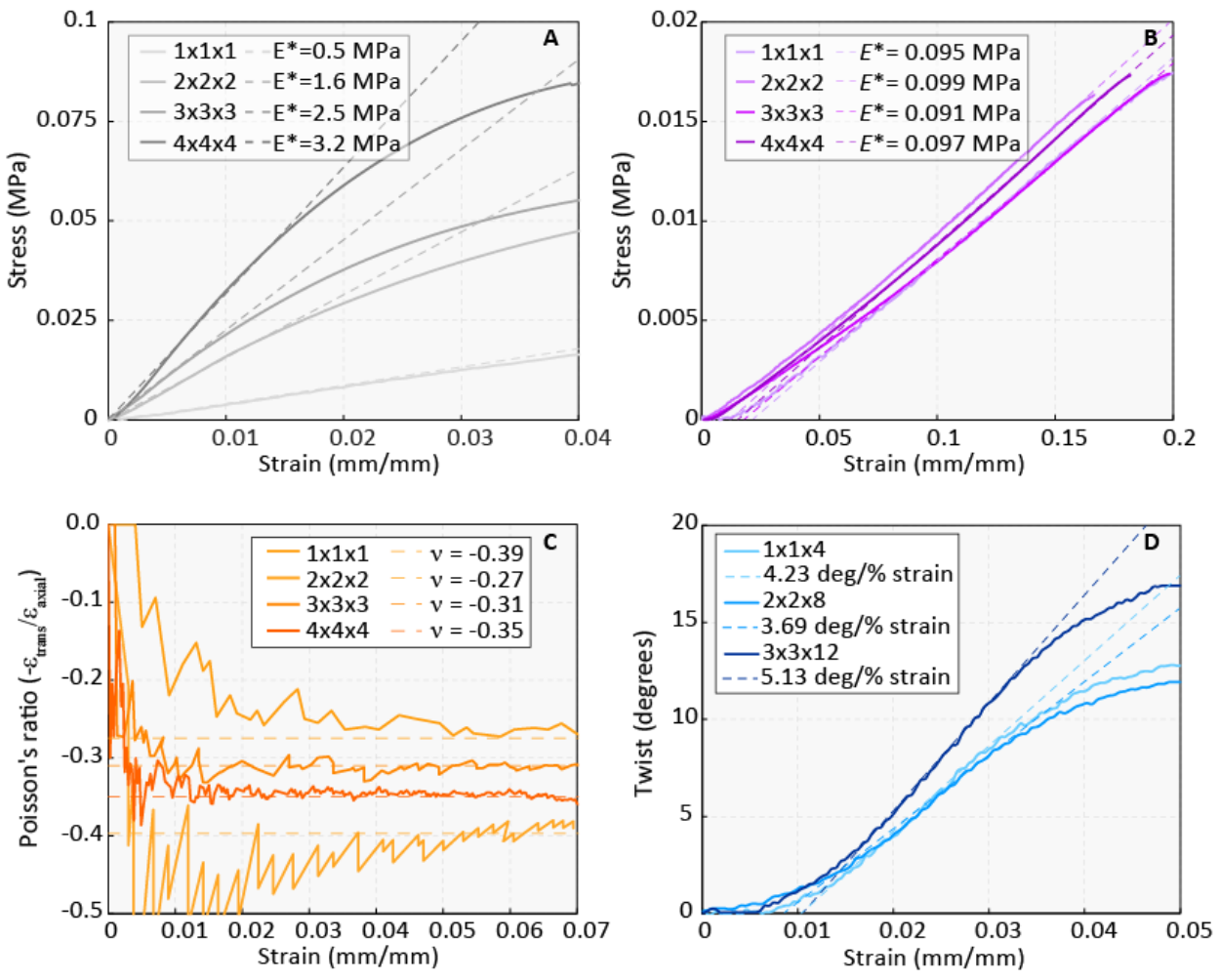
136

137 **Figure S 6: Comparison of numerical modeling methods and experimental results.** We see good
 138 agreement between experiment, fully meshed FEA (NASTRAN), as-built beam model, and
 139 theoretical beam model, in terms of deformed shape to same applied strain, and von mises stress
 140 distribution, noting some concentrations visible in simplified model.

141

142

143 **Experimental results**



144

145

146 **Figure S 7: Experimental results. A) Rigid, B) Compliant, C) Auxetic, D) Chiral.**

147

148

149

Table S1: Assembly metrics

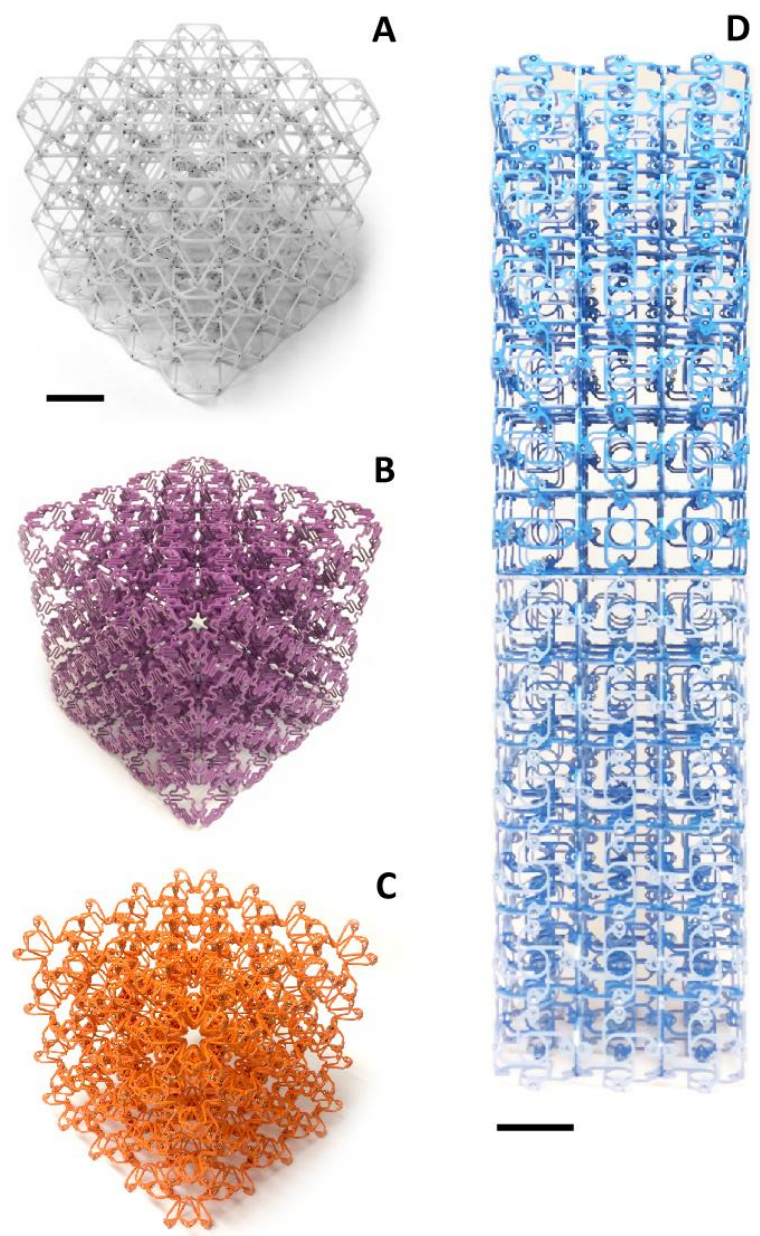
Specimen cube voxel width <i>n</i>	Total voxels	Total Rivets	Avg rivets/voxel	Time/voxel (min)	Total time (min)	cm ³ /hr	g/hr
1	1	12	12	1.5	1.5	16,876	500
2	8	144	18	2.25	18	11,250	333
3	27	540	20	2.5	67.5	10,125	300
4	64	1344	21	2.625	168	9,643	285
5*	125	2700	21.6	2.7	337.5	9,375	277
10*	1000	22800	22.8	2.85	2850	8,882	263
<i>N</i> *	<i>N</i> ³	<i>N</i> ³ *12 + [<i>N</i> ² *(3(<i>N</i> -1))]*4	24	3	3* <i>N</i> ³	8,440	250

150 * = projected (not built), Avg Rivet time = 7.5s, Voxel mass = 12.5g, Voxel vol = 422 cm³

151

152

153



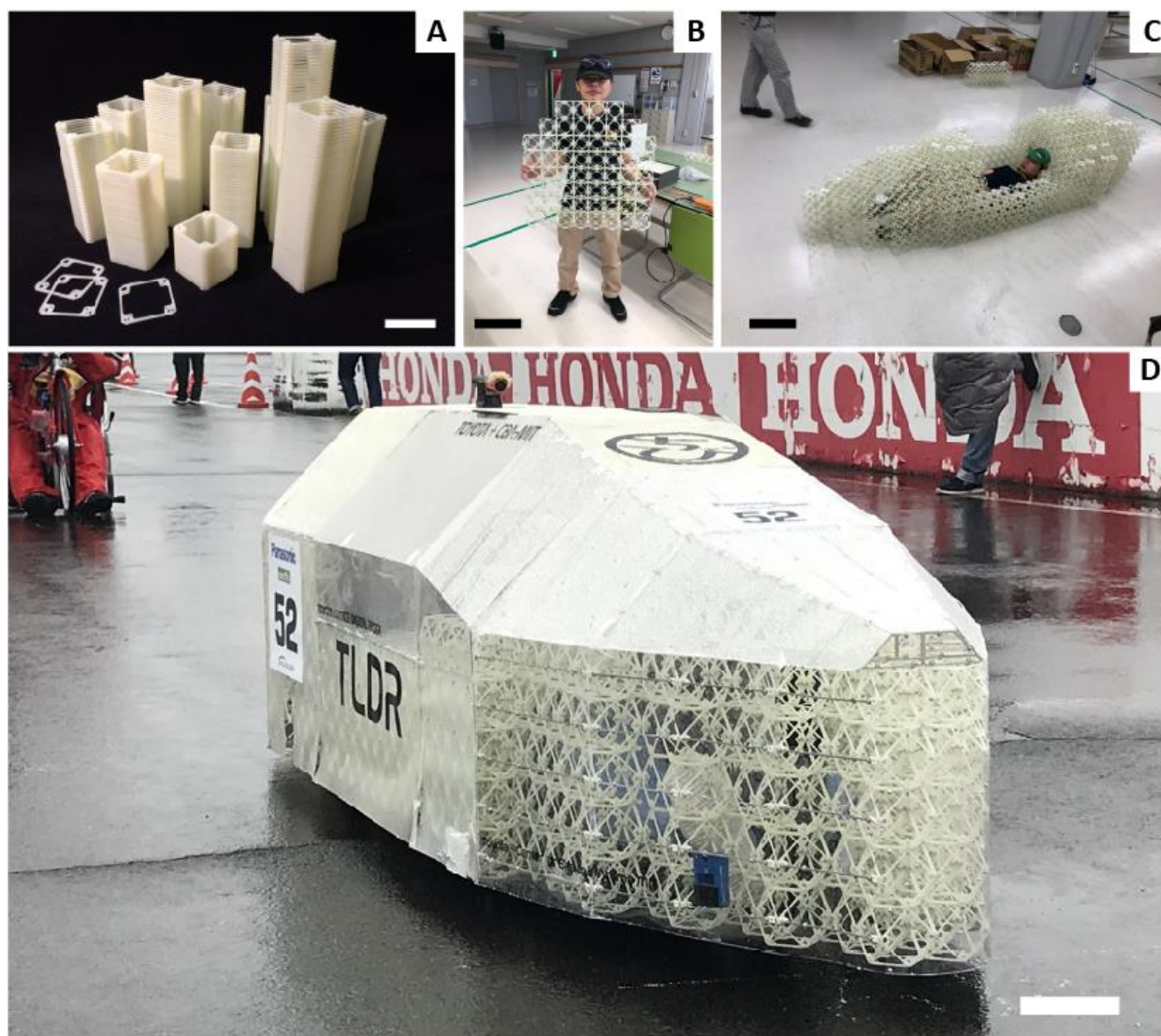
155
156 **Figure S 8: As-built lattice specimens. A) Rigid, B) Compliant, C) Auxetic, D) Chiral. Scale bar:**
157 **75mm.**

158

159

160 **Macro-scale structural application**

161



162

163 **Figure S 9: Large scale Application of discretely assembled mechanical metamaterial as a car**
164 **frame.** A) Mass produced parts, B) Assembled layer, C) Completed frame without subsystems, D)
165 Supermileage vehicle in operation. Scale bars A) 75mm, B) 225mm, C) 225mm, D) 150mm.

166 *Image credit: Kohshi Katoh, Toyota Motor Corporation.*

167